Master's thesis

NTNU
Norwegian University of Science and Technology
Faculty of Natural Sciences

Andrea Åvik Larsen

Optimization of Stöber Method to Control Morphology and Enhance Stability of Amine-Functionalized Silica Coated Iron Oxide Nanoparticles

Master's thesis in Chemical Engineering
Supervisor: Sulalit Bandyopadhyay
Co-supervisor: Zeeshan Ali
June 2023

NTNU
Norwegian University of
Science and Technology

Andrea Åvik Larsen

Optimization of Stöber Method to Control Morphology and Enhance Stability of Amine-Functionalized Silica Coated Iron Oxide Nanoparticles

Master's thesis in Chemical Engineering
Supervisor: Sulalit Bandyopadhyay
Co-supervisor: Zeeshan Ali
June 2023

Norwegian University of Science and Technology
Faculty of Natural Sciences

NTNU
Norwegian University of
Science and Technology

Abstract

Silica coated iron oxide nanoparticles (IONPs) possess a remarkable combination of properties, including superparamagnetism, excellent stability in aqueous solutions, easy surface functionalization, and biocompatibility, which makes them especially promising for various biomedical applications such as therapeutics and diagnostics. However, precise control over the sizes and morphologies of silica coated IONPs is crucial for their performance.

In our research group, a modified Stöber method has been explored for the silica coating of IONPs. A study conducted by Ali *et al.* [1], revealed that reaction parameters such as the nature of solvent, the mass ratio of IONPs to silica precursor, surface groups of IONPs, and concentration of catalyst, resulted in distinct morphologies and particle sizes. However, there has been a lack of systematic research dedicated to examining input parameters including the type of silica precursor and volume of solvent.

In this study, a combination of tetraethyl orthosilicate (TEOS) and 3-aminopropyl triethoxysilane (APTES) was utilized as silica precursors, resulting silica coated IONPs which are directly surface functionalized with primary amine groups. An extensive synthetic study was conducted, involving detailed characterization to assess the impact of varying the mass ratio of TEOS to APTES, the type of IONPs, and the solvent volume on the size, morphology, surface properties, and magnetic responses of silica coated IONPs. As a part of the work, a colorimetric ninhydrin assay was carried out to analyze the quantity of surface amine groups.

The results demonstrated that the combination of TEOS and APTES is important for achieving a suitable silica coating. The concentration of APTES significantly affected the particle morphology, with higher concentrations leading to the formation of large silica coated IONPs, silica particles, and IONP aggregates with a thin silica layer. Lower concentrations resulted in the formation of individual silica coated IONPs with sizes ranging from $\sim$ 60 nm - 100 nm. The type of IONPs and solvent volume utilized had relatively minor effects compared to the ratio of TEOS to APTES. The developed ninhydrin assay confirmed the presence of primary amine groups on the surfaces of the silica coated IONPs. However, the unusually high amine group content detected raises concerns about the reliability of the assay, requiring further investigations.

Sammendrag

Silikabelagte jernoksidnanopartikler har en bemerkelsesverdig kombinasjon av egenskaper, inkludert superparamagnetisme, utmerket stabilitet i vandige løsninger, enkel overflatefunksjonalisering og biokompatibilitet, noe som gjør dem spesielt lovende for ulike biomedisinske applikasjoner som terapeutikk og diagnostikk. Derimot er nøyaktig kontroll over størrelsene og morfologiene til silikabelagte jernoksidnanopartikler avgjørende for ytelsen deres.

I vår forskningsgruppe har en modifisert Stöber-metode blitt utforsket for silikabelegging av jernoksidnanopartikler. Et studie utført av Ali *et al.*[1] avdekket at reaksjonsparametere som løsningsmidlets natur, masseforholdet mellom jernoksidnanopartikler og silika forløper, overflategrupper på jernoksidnanopartikler og konsentrasjon av katalysator, resulterte i distinkte morfologier og partikkelstørrelser. Imidlertid har det vært mangel på systematisk forskning dedikert til å undersøke inngangsparametere, inkludert typen silikaforløper og volum av løsemiddel.

I dette studiet ble en kombinasjon av tetraetylortosilikat (TEOS) og 3-aminopropyl trietoksysilan (APTES) brukt som silikaforløpere, noe som resulterte i silikabelagte jernoksidnanopartikler som er direkte overflatefunksjonaliserte med primære amingrupper. Et omfattende syntetisk studie ble utført, som involverte detaljert karakterisering for å vurdere virkningen av å variere masseforholdet mellom TEOS og APTES, typen jernoksidnanopartikler og løsemiddelvolumet på størrelsen, morfologien, overflateegenskapene og de magnetiske responsene til silikabelagte jernoksidnanopartikler. Som en del av arbeidet ble det utført en kolorimetrisk ninhydrinanalyse for å analysere mengden av overflateamingrupper.

Resultatene viste at kombinasjonen av TEOS og APTES er viktig for å oppnå et passende silikabelegg. Konsentrasjonen av APTES påvirket partikkelmorfologien betydelig, hvor høyere konsentrasjoner førte til dannelse av store silikabelagte jernoksidnanopartikler, silikapartikler og aggregater av jernoksidnanopartikler med et tynt silikalag. Lavere konsentrasjoner resulterte i dannelsen av individuelle silikabelagte jernoksidnanopartikler med størrelser fra $\sim$ 60 nm - 100 nm. Typen jernoksidnanopartikler og løsemiddelvolum som ble brukt hadde relativt små effekter sammenlignet med forholdet mellom TEOS og APTES. Den utviklede ninhydrinanalysen

bekreftet tilstedeværelsen av primære amingrupper på overflatene til de silikabelagte jernoksid-nanopartiklene. Imidlertid gir det oppdagede uvanlige høye amingruppeinnholdet en bekymring for påliteligheten til analysen, og krever videre undersøkelser.

Preface

This master's thesis was written as a completion of the five year master's degree program in Chemical Engineering and Biotechnology at NTNU, with a main profile in Chemical Engineering. The work was conducted during the spring semester of 2023 under the supervision of Dr. Sulalit Bandyopadhyay at the Department of Chemical Engineering. The specialization project with the title '*Study of Particle Sizes and Morphologies of Silica Coated Iron Oxide Nanoparticles Synthesized by Thermal Decomposition*', completed in December 2022 by the same author, was utilized as a preparation for this study. Certain sections of the theory and methodology are strongly inspired by or partly derived from that work.

First of all, I want to express my gratitude to my supervisor Dr. Sulalit Bandyopadhyay for giving me the opportunity to work on this project, and for his exceptional knowledge and valuable guidance throughout the process. I want to thank my co-supervisor and PhD candidate Zeeshan Ali for all of the helpful discussions, support, and practical advice that have been useful for all of the experiments conducted this semester. Thanks to everyone in the Particle Engineering Centre Team for the supportive environment and the many interesting conversations. It has been a pleasure getting to know you all. Finally, I want to thank my friends and family for always believing in me and supporting my decisions.

Contents

Figures

Nomenclature

Acronyms and Abbreviations

APTES	3-Aminopropyl triethoxysilane
CNT	Classical Nucleation Theory
CP-IONPs	Co-Precipitation Iron Oxide Nanoparticles
DLS	Dynamic Light Scattering
EDS	Energy Dispersive X-ray Spectroscopy
IEP	Isoelectric Point
IONPs	Iron Oxide Nanoparticles
MQ	MilliQ
NMR	Nuclear Magnetic Resonance
SSA	Specific Surface Area
STEM	Scanning Transmission Electron Microscopy
TD-IONPs	Thermal Decomposition Iron Oxide Nanoparticles
TEM	Transmission Electron Microscopy
TEOS	Tetraethyl orthosilicate
TGA	Thermogravimetric Analysis
TREG	Triethylene glycol
UV-vis	Ultraviolet-visible
VSM	Vibrating Sample Magnetometer
XPS	X-ray Photoelectron Spectroscopy

Units and Symbols

$\sim$	approximately
ζ	zeta
%	percent
^{o}C	degree Celsius
μmol	micro mol
μL	micro liter
cm^3	cubic centimeter
g	gram
nm	nanometer
nm^2	square nanometer
nm^3	cubic nanometer
M	molar / mol per liter
mg	milli gram
min	minute(s)
mL	milli liter
mM	milli molar
mmol	milli mol
mV	milli volt
pH	negative decadic logarithm of the hydrogen ion activity
rpm	revolutions per minute
sec	second(s)
wt%	weight percent

Chapter 1

Introduction

Nanoparticles are at the forefront of the exponential growth of nanotechnology, where their size-dependent properties render them superior in numerous of research fields [2]. In this context, magnetic nanoparticles possess important qualities that make them especially attractive for biomedical applications, including magnetic resonance imagining [3], magnetic hypothermia [4], targeted drug delivery [5, 6], and bio-sensing and diagnostics [7]. Recently, researchers at NTNU developed a method for detecting the SARS-CoV-2 virus by using magnetic magnetite nanoparticles [8]. Magnetic iron oxide nanoparticles (IONPs), such as magnetite (Fe_3O_4), are very promising as they display superparamagnetic features, low cytotoxicity and can be generated using various synthetic processes [9]. The functionality of iron oxide nanoparticles is directly related to their size, shape, coating, and stability, which can be controlled by tuning their synthetic conditions [10]. Thermal decomposition of iron precursors in a high boiling solvent is a common technique that permits size-controlled synthesis of monodisperse nanoparticles by separating the nucleation and growth phases [11]. Desired particle requirements for biomedical applications are typically high magnetic saturations, overall narrow particle size distributions, and excellent stability. Iron oxide nanoparticles have a large surface area to volume ratio, and consequently, they tend to aggregate in order to reduce their surface energies. Additionally, bare iron oxide nanoparticles possess high chemical reactivity and are readily oxidized, causing loss of magnetism and dispersibility. In order to preserve the stability of iron oxide nanoparticles and tune their magnetic saturation, it is crucial to apply suitable surface coatings [12]. Silica (SiO_2) has proven to be an effective coating material for iron oxide nanoparticles through a process known as silanization. Colloidal silica is an inorganic and biocompatible material, that provides several possibilities for specific surface functionalization [13]. Generally, a silica surface can be functionalized either by co-condensation, in which functional species are added directly to the silica matrix during the silica coating process, or by post-synthetic modification, in which functional groups are covalently attached to silica through the silanol groups on the surface [14].

One of the most well-known methods to prepare silica coated IONPs is based on the Stöber process in which silica is formed through the hydrolysis and condensation of tetraethyl orthosilicate (TEOS) in an aqueous solution consisting of ethanol and ammonia [15]. Variations of this method have been explored and extensive studies have been conducted to tune the final particle properties. During the specialization project, written in fall 2022, it was developed a modified Stöber protocol for silica coating of iron oxide nanoparticles. The silanization was performed as a co-condensation approach in which tetraethyl orthosilicate (TEOS) and 3-aminopropyl triethoxysilane (APTES) were combined as silica precursors. The results yielded superparamagnetic, amine-functionalized silica coated IONPs down to $\sim$100 nm in size.

This study aims to improve the silanization process, which was developed during the specialization project, by investigating the influence of specific reaction parameters on the particle properties. This optimization process will lay the groundwork for the synthesis of silica coated IONPs with tailored characteristics for applications in various fields. The specific synthesis generates nanoparticles with unique properties as they are magnetically separable in the presence of an external magnetic field, and colloidally stable in aqueous solutions. The combination of TEOS and APTES as silica precursors provides a surface chemistry rich in both hydroxyl (-OH) and primary amine (-NH_2) groups. However, the chemical stability and reactivity of the coated surface are dependent on the density of functional groups, which must be quantified. In this context, this work specifically focuses on the establishment of a colorimetric ninhydrin assay to quantify the surface amine groups present on the silica coated IONPs.

This thesis consists of five chapters, with the current Chapter 1 being the introduction and motivation behind the work. Chapter 2 provides an overview of the theory behind crystallization and nanoparticle design, followed by literature related to the synthesis and properties of IONPs and silica coated IONPs. Chapter 3 outlines the materials and protocols of the synthesized particles. Chapter 4 presents the results obtained, followed by thorough discussions. Finally, Chapter 5, provides a summary of the key findings of the thesis and suggests work for future research.

Chapter 2

Theory and Literature Review

This chapter aims to establish the essential theoretical framework required to understand and support the conducted work. It will begin by introducing the fundamental principles of the crystallization of nanoparticles. This knowledge will lay the groundwork for the subsequent section, which will discuss iron oxide nanoparticles (IONPs), their unique magnetic properties, and specific synthetic approaches. Additionally, the chapter will explore the topic of silica coating for IONPs, focusing particularly on the Stöber method. Lastly, the concluding part of this chapter will cover the amine functionalization of silica coatings and the quantification of amine groups. It should be noted that parts of this chapter are highly inspired by previous work.

2.1 Crystallization

Crystallization is a phase transition process that converts matter in a high free energy state into solid crystals with an organized internal arrangement of material units and minimized free energy. The process occurs in two main steps, namely nucleation and crystal growth, where the state of supersaturation is the essential driving force in the classical theory of crystallization. The formation of a crystal phase is influenced by both thermodynamic and kinetic factors, providing a range of potential pathways for crystallization to occur [16, 17].

2.1.1 Supersaturation

Supersaturation is the most significant parameter to control the mechanisms and kinetics of solution-based crystallization processes. A solution is considered saturated when it is in thermodynamic equilibrium with the solid phase of a solute at a specified reference temperature and pressure. Activity-based supersaturation arises when the activity of a solute exceeds the activity at thermodynamic equilibrium. This excess free energy forces crystallization to happen. More specifically, supersaturation originates from the difference in the chemical potential between a

given substance in the solution (state 1) and in the crystal phase (state 2), expressed as [16, 17]:

$$\Delta\mu = \mu_1 - \mu_2 \tag{2.1}$$

Chemical potential, μ, is represented by:

$$\mu = \mu_0 + RTln(a) \tag{2.2}$$

where μ_0 is the standard chemical potential, R is the universal gas constant, T is the temperature, and a is the activity. By inserting Equation 2.2 into 2.1, the difference in chemical potential, $\Delta\mu$, can be expressed as:

$$\Delta\mu = RTln\left(\frac{a}{a^*}\right) \tag{2.3}$$

where a is the activity of the solute in an arbitrary state, while a^* is the activity of the same solute at equilibrium. The activity ratio from Equation 2.3 is defined as supersaturation, S:

$$S = \left(\frac{a}{a^*}\right) \tag{2.4}$$

which measures the tendency of the system to precipitate. When $S > 1$, i.e. supersaturated state, the difference in chemical potential is larger than zero, and spontaneous crystallization occurs. Activity can be defined as:

$$a = c\gamma_a \tag{2.5}$$

where c is the concentration of a solute, and γ_a is the activity coefficient, which describes the deviation from an ideal solution. The activity coefficient of soluble electrolytes is influenced by factors such as the ionic strength of the solution, as well as the size and charge of all the components involved. In the case of a precipitation reaction involving magnetite (Fe_3O_4), the degree of supersaturation, as indicated in Equation 2.4, can be expressed in terms of the solubility product as [18]:

$$S_{magnetite} = \left(\frac{a_{Fe^{3+}}\, a_{Fe^{2+}}\, a_{OH^-}}{K_{sp}}\right)^{\frac{1}{\nu}} \tag{2.6}$$

where a represents the activity of the ions forming magnetite, K_{sp} is the temperature dependent solubility product of the solute and ν is the number of moles of ions per mole of solute.

2.1.2 Classical Nucleation

Nucleation represents the initial appearance of a new phase in a solution, known as nuclei. Several theories for modeling nucleation have been proposed during the last decades [19]. The classical nucleation theory (CNT) is the most common theoretical framework used to study the kinetics of nucleation on a thermodynamic basis. According to CNT, nuclei are formed through dynamic and

stochastic association of monomeric units [17]. In CNT, primary nucleation refers to homogeneous or heterogeneous nucleation, in systems that do not contain the crystalline matter in advance. Homogeneous nucleation appears on its own in the absence of a solid surface, while heterogeneous nucleation is induced by a foreign inhomogeneity in the system, such as container surfaces or impurities, and this event occurs more readily for primary nucleation systems. Secondary nucleation is induced by crystals of the solute present in the solution and requires shear forces to be active on the particles, which typically become effective at the micron scale [16, 17].

The CNT is easiest explained considering the Gibbs free energy change of a homogeneous nucleating system of a spherical nucleus, as represented by Figure 2.1. The total Gibbs free energy, ΔG, between a formed nucleus and the solute in the solution is determined by the combined contributions of free energy change of surface formation, ΔG_S, and phase transformation, also called volume free energy, ΔG_V. This is given by [16, 17]:

$$\Delta G = \Delta G_V + \Delta G_S \tag{2.7}$$

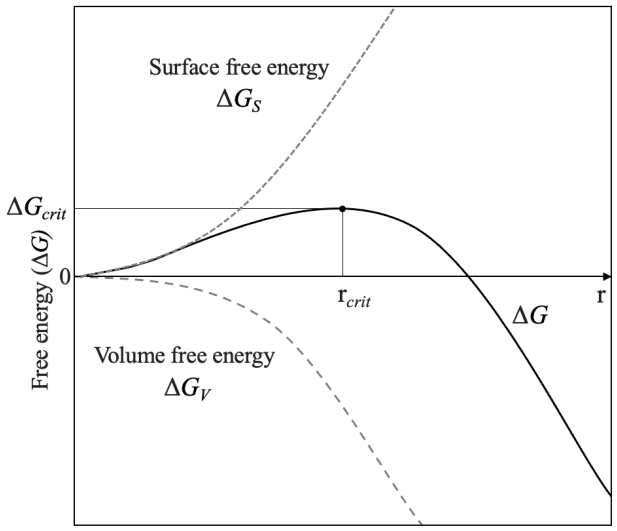

Figure 2.1: Gibbs free energy diagram for homogeneous nucleation as a function of radius for a spherical nucleus. The Figure is inspired by Mullin [16].

As seen from Figure 2.1, the energetic costs of creating a surface dominate over excess free energy reduction from phase transformation at small sizes, thus creating energetically unfavorable clusters. When the system approaches the critical radius, r_{crit}, the volume free energy starts to balance out the positive surface contribution. At this point, the attachment of monomeric units overcome the free energy barrier which results in a phase separation and formation of a stable nucleus. The volume and surface free energy are directly related to the volume and surface area of the nucleus. Consequently, Equation 2.7 can be derived to:

$$\Delta G = \frac{4}{3}\pi r^3 \Delta G_v + 4\pi r^2 \gamma \tag{2.8}$$

where γ is the surface free energy of the liquid-solid interface. ΔG_v is equal to the driving force for phase transformation, i.e. the change in chemical potential, and can be written in terms of supersaturation, S, as followed:

$$\Delta G_v = \Delta \mu_v = -\frac{\nu k_B T \ln S}{v_m} \tag{2.9}$$

where v_m is the molecular volume, ν is moles of ions per mole of solute, k_B is Boltzmann constant and T is the temperature. The critical radius, r_{crit}, is determined by inserting Equation 2.9 into 2.8, and differentiating ΔG with respect to r and setting it to zero. This gives:

$$r_{crit} = -\frac{2\gamma}{\Delta G_v} = \frac{2\gamma v_m}{\nu k_B T \ln S} \tag{2.10}$$

The corresponding critical Gibbs free energy barrier, ΔG_{crit}, is hence:

$$\Delta G_{crit} = \frac{16\pi\gamma^3}{3\Delta G_v^2} = \frac{16\pi\gamma^3 v_m^2}{3k_B^3 T^3 (\nu \ln S)^2} \tag{2.11}$$

Consequently, from Equation 2.10 and 2.11, it is shown that interfacial energy, temperature, and supersaturation are parameters that affect the energy barrier, and consequently the probability and rate of nucleation. In the event of heterogeneous nucleation, the surface free energy term, ΔG_S, reduces due to lower interfacial energy between the nucleus and an existing surface. This results in a lower free energy barrier for heterogeneous nucleation compared to homogeneous nucleation, while the critical radius remains the same [16, 17].

According to CNT, the nucleation rate, J, represents the number of stable nuclei formed per unit of time and volume. It can be mathematically represented in the form of the Arrhenius reaction rate equation as followed:

$$J = \exp\left(\frac{-\Delta G_{crit}}{k_B T}\right) \tag{2.12}$$

where A covers the kinetic factors for nucleation, given by:

$$A = z\, f\, C_0 \tag{2.13}$$

The Zeldovich factor, z, corrects for nuclei that dissolve instead of grow, f is the attachment frequency of monomers to the nucleus and C_0 represents the concentration of nucleation sites [16, 17].

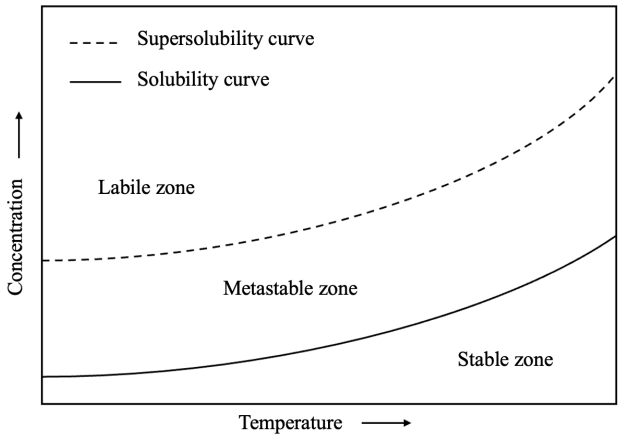

Figure 2.2: Illustration of the solubility and super solubility curves, and the stable, metastable and labile zones for a solid that dissolves endothermically. The Figure is inspired by Panagiotou and Fisher [20]

The Gibbs free energy barrier and rate of nucleation depend largely on the level of supersaturation. Figure 2.2 demonstrates concentration-based solubility and supersaturation zones as a function of temperature. Below the solubility curve, in the stable zone, crystallization is impossible and the system is undersaturated. Supersaturation is established once the system crosses the solubility curve into the metastable zone. Despite being supersaturated, metastable solutions can stay in this state for a significant period of time before undergoing nucleation. In the labile zone, uncontrolled spontaneous nucleation and growth occur as a result of thermodynamic instability. Consequently, it can be challenging to prevent rapid and uncontrolled nucleation, and the metastable zone is typically where controlled crystallization operations are carried out [16, 17].

2.1.3 Crystal Growth and Morphology

Crystal growth is the increase in size of nuclei and crystalline particles. According to the classical theory, supersaturation is the essential growth-promoting force and growth occurs by the attachment of monomeric building units from the solution to the crystalline structure. The growth process occurs at a lower energy barrier compared to nucleation. Once a sufficient number of nuclei have formed, the supersaturation can be consumed by growth, lowering the free energy of the system. The rate of growth, R, can be described by [17]:

$$R = k(S-1)^g \tag{2.14}$$

where k is the growth rate constant, S is the activity-based supersaturation and g is the growth order depending on the growth mechanism. Generally, growth is controlled by two mechanisms: diffusion of growth units from solution to the crystal surface, followed by attachment of monomers into energetically favored kink sites on the crystal surface. Both of these steps can be rate limiting,

resulting in the terms diffusion-controlled and surface reaction-controlled growth [16, 17].

Different particle morphologies can be developed, depending on the growth rate and mechanism, which is highly regulated by the level of supersaturation and generation of active growth sites. Generally, reaction-controlled growth is obtained by lowering the driving force, which limits the number of kink sites and provides smooth and well-defined faceted particles. On the contrary, very high supersaturation levels will generate numerous active sites, which leads to rapid surface incorporations and diffusion-limited growth. This promotes spherical and rougher particle surfaces, where the growth on certain facets becomes less significant [16, 17].

2.1.4 Particle Size and Size Distribution

The LaMer mechanism, proposed by LaMer and Dinegar [21] in 1950, is a classical theoretical model that outlines the formation of monodisperse particles from crystallization. The theory is illustrated by Figure 2.3, which represents how the monomer concentration, and accordingly supersaturation, changes in a system as a function of reaction time. (I) Initially, the concentration of monomers in the solution increases rapidly above the critical nucleation barrier. (II) The system undergoes instantaneous self-nucleation, called burst-nucleation, which quickly reduces the concentration of free monomers in solution below the limit where nucleation terminates. (III) Subsequently, free monomers in solution are consumed by diffusion-controlled growth of nuclei into particles with a narrow particle size distribution [22]. The effective separation of burst-nucleation

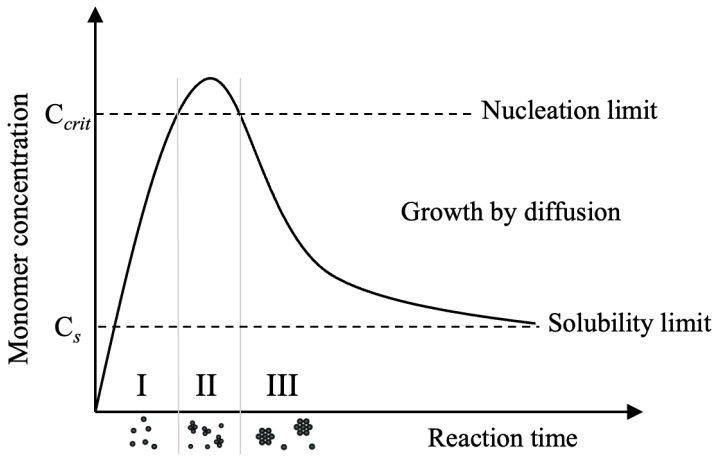

Figure 2.3: The LaMer diagram showing the separation of nucleation and growth. The Figure is inspired by Zhao [23].

from crystal growth is the key to a controlled, uniform particle size. When nuclei are produced over a short period of time, they will be formed under equivalent conditions and attain a similar size. Subsequently, they will grow under the same conditions and duration, which favor monodisperse particles.

In general, the size of a crystal is determined by the two competing mechanisms of crystal nucleation and crystal growth over the consumption of supersaturation. There are several approaches that can be employed to tune the final particle sizes, which primarily depend on factors controlling the kinetics of nucleation and growth. For instance, a high nucleation rate can be achieved by rapidly increasing the level of supersaturation in the system. This typically allows a greater number of nuclei to form before the growth process becomes dominant, compared to a slower nucleation rate. As a result, the remaining monomeric units for growth will attach to a larger fraction of nuclei, causing the formation of many small particles. On the contrary, fewer nucleation events would lead to fewer but larger particles [24].

2.1.5 Electrostatic Stabilization of Nanoparticles

Particles at the nanoscale have a high surface energy, which make them unstable and prone to aggregation at short interparticle distances. In this work, aggregation is referred to as the reversible clustering of particles as a result of physical attraction forces, such as van der Waals, electrostatic, or magnetic forces. Electrostatic or steric surface stabilization can prevent the aggregation behavior of nanoparticles. Surface absorption of charged molecules, such as citrate ions, will cause electrostatic repulsion between particles, whereas the absorption of larger molecules, such as polymers, typically generates steric stabilization [24].

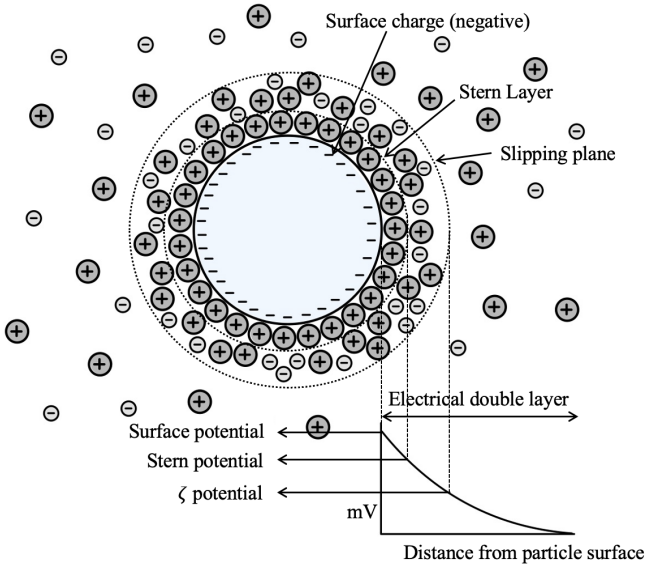

Figure 2.4: The electric double layer for a negatively charged particle. The Figure is inspired by Park *et al.* [25].

The electric double layer, provided in Figure 2.4, plays an important role in the electrostatic stabilization of colloids. Nanoparticles dispersed in a solution will possess a surface potential, due to reactions involving functional groups or the absorption of ions from the solution. For instance,

acidic or basic functional surface groups will undergo dissociation and protonation in contact with water, leading to the formation of negative and positive surface charges, respectively. However, the equilibrium of dissociation and protonation is highly dependent on the pH of the surrounding medium, which consequently influences the surface charge [26]. An electric double layer consists of three parts: charged ions at the particle surface, a compact inner Stern layer with closely attached counterions, and a diffuse outer layer of loosely attached ions. The electric potential decreases with increasing distance from the particle surface, and the total magnitude and thickness of the electric double layer are directly related to solution properties such as pH and ionic strength [27]. When colloidal particles move in a solution, a layer of ions will constantly follow the particles as one entity. The boundary of this layer is called the slipping plane, and the corresponding electric potential between the slipping plane and the bulk solution is specified as the zeta potential (ζ-potential). Therefore, the electric stabilization of a dispersion can be assessed by measuring the zeta potential. The isoelectric point (IEP) is known as the pH level where the zeta potential is equal to zero and the electric repulsion between colloids is at its lowest. In general, higher absolute zeta potential values indicate stronger electrostatic repulsive forces between particles, which reduce the likelihood of particle aggregation. A suspension of nanoparticles is typically considered electrostatically stable when it has an absolute zeta potential value of at least 30 mV [25, 28].

2.2 Iron Oxide Nanoparticles

Nanoparticles exhibit unique and controllable properties that are distinct from those they display at the macroscopic scale. When particles are reduced in size, the ratio of surface atoms to massive atoms rises significantly, causing the surface atoms to dominate the performance of the nanoparticle. This allows nanoparticles to possess outstanding optical, electrical, and magnetic behaviors, as they are sufficiently tiny to confine their electrons and generate quantum effects [29]. Iron oxide nanoparticles (IONPs) are compounds of iron and oxygen, with magnetite (Fe_3O_4) and its oxidized form, maghemite (γ-Fe_2O_3), being the most prevalent forms. Depending on their different crystal structures, IONPs possess varying magnetic properties.

2.2.1 Magnetic Properties

Magnetic properties are a result of the magnetic moments associated with the motion of electrons in atoms. Each individual atom possesses a magnetic moment, which is a vector quantity that includes both magnitude and direction. The alignment of these magnetic moments within a material leads to the overall magnetic effect observed at the macroscopic scale [30].

As illustrated in Figure 2.5, various magnetic states can arise in different magnetic materials. In the paramagnetic state, each of the magnetic moments of individual atoms is arbitrarily aligned with respect to each other, resulting in a net magnetic moment of zero. When a paramagnetic

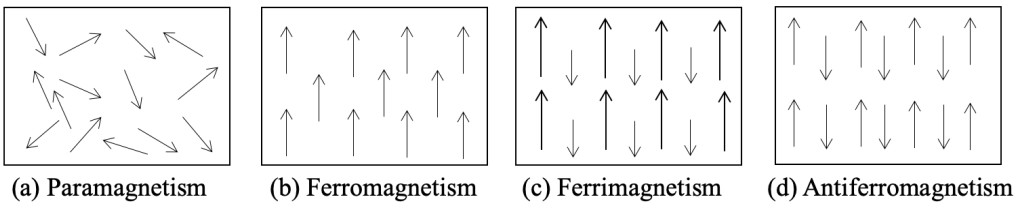

Figure 2.5: Allignment of atomic magnetic moments in different magnetic states: (a) paramagnetic, (b) ferromagnetic, (c) ferrimagnetic and (d) antiferromagnetic. The Figure is inspired by Teja *et al.* [30].

material is exposed to an external magnetic field, some of the magnetic moments will align in the direction of the field, causing a small net magnetic moment to arise. In contrast, a ferromagnetic material exhibits alignment of all individual magnetic moments in the presence of an external field, resulting in a large net magnetic moment. Even after the field is removed, the material retains some net magnetic moment. In ferrimagnetic and antiferromagnetic materials, neighboring magnetic moments align in antiparallel arrangements, but with different outcomes. In the ferrimagnetic state, the antiparallel magnetic moments have varying strengths, leading to a positive net magnetic moment. On the other hand, in the antiferromagnetic state, the antiparallel magnetic moments have equal magnitudes, resulting in no net magnetic moment. The arrangement of magnetic moments in each of these states is the result of favorable exchange interactions within the material. At higher temperatures, the ordered arrangement of magnetic moments can be disrupted due to thermal fluctuations, causing a decrease in magnetization. The transition temperature where this event occurs is known as the Curie temperature for ferromagnetic and ferrimagnetic compounds, and the Néel temperature for antiferromagnetic substances [30].

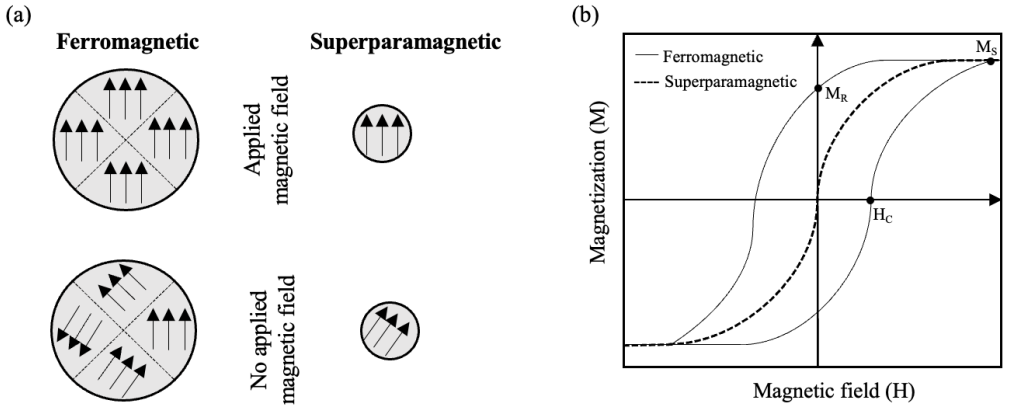

Figure 2.6: Different (a) domains and (b) magnetization curves for ferromagnetic and superparamagnetic materials. The Figure is inspired by Teja *et al.* [30].

As seen in Figure 2.6 (a), ferromagnetic bulk materials contain distinct domains where atomic magnetic moments are precisely aligned. When the size of the material is reduced below a critical

value, typically less than 15 nm, only a single domain is detected, and the material may exhibit superparamagnetic behavior [17]. Figure 2.6 (b) illustrates how the magnetization value in ferromagnetic and superparamagnetic materials increases until it reaches a saturation value, M_S, when an external magnetic field of strength, H, is applied. In a ferromagnet, even after the field is removed and H returns to zero, not all domains revert to their original orientations, resulting in a remnant magnetization, M_R. To eliminate the remnant magnetization, a coercive field, H_c, in the opposite direction to the initial applied field is required. However, a superparamagnetic material, displays zero coercivity, implying that it instantly demagnetizes when the external field is removed and the magnetization curve shows no hysteresis loop [30]. Therefore, magnetic fields can effectively manipulate superparamagnetic particles, as they easily separate in the presence of a field and have less tendency to aggregate in the absence of it.

Bulk magnetite exhibits ferrimagnetic properties at room temperature, and when the temperature rises above its Curie temperature, typically between 500 °C and 600 °C, it transforms to a paramagnetic state [31]. On the other hand, magnetite nanoparticles with sizes below approximately 20 nm display single-domain behavior and exhibit superparamagnetic properties at ambient temperature [32]. This exceptional magnetic characteristic makes them highly suitable for a wide range of applications, including magnetic resonance imagining [3], magnetic hyperthermia therapy [4], targeted drug delivery [5], bio-sensing and diagnosis [7], catalysis [33], batteries [34], and as sorbents for pollutants and water treatment [35]. Along with their superparamagnetic properties and simple separation methodology, iron oxide nanoparticles, such as magnetite, demonstrate low toxicity in the human body, making them particularly advantageous for biomedical applications [2, 36]. By adjusting synthetic conditions and controlling parameters like particle size, morphology, stability, and composition, it is possible to successfully produce iron oxide nanoparticles with desired magnetic characteristics.

2.2.2 Synthesis by Thermal Decomposition

Thermal decomposition is a widely used chemical technique to produce IONPs, due to the monodispersity of the generated particles. IONPs are synthesized by decomposing iron precursors in high-boiling organic solvents containing surfactants at high temperatures (> 230 ^{o}C) [37]. The key behind the controlled narrow size distribution observed in thermal decomposition is the effective separation of burst nucleation from particle growth. The underlying principles are explained by the LaMer model [21], described in Section 2.1.4. In this model, nuclei are formed rapidly and nucleation terminates when growth begins, making it easy to achieve uniform growth, and as a result, a narrow particle size distribution.

Iron olate, iron pentacarbonyl, and iron acetylacetonate are commonly used as iron precursors in thermal decomposition, while oleic acid and oleylamine are typically employed as surfactants for stabilization [38–40]. However, nanoparticles stabilized with lipophilic substances, such as

oleic acid, are only stable in hydrophobic media. This serves as a limitation for applications and requires an intermediate phase transfer step to aqueous media [41]. Recently, it was developed a direct synthesis of water-dispersible magnetite nanoparticles, reported by Wan *et al.* [42] and Maity *et al.* [40] respectively. The synthesis involves the decomposition of iron(III) acetylacetonate in hydrophilic triethylene glycol (TREG), which acts as both a high-boiling solvent and a stabilizer. According to Maity *et al.*, the particles exhibited a spherical morphology, displayed a relatively uniform size distribution with an average TEM size of 11 nm, and demonstrated superparamagnetic properties.

2.2.3 Synthesis by Co-precipitation

Co-precipitation is another widely used and traditional method for synthesizing IONPs, alongside thermal decomposition. In co-precipitation, IONPs are formed from aqueous iron salt (Fe^{2+}/Fe^{3+}) solutions by the addition of a base, at room temperature or elevated temperatures. The main reaction for the formation of magnetite from co-precipitation is presented by [43]:

$$Fe^{2+} + 2Fe^{3+} + 8OH^{-} \rightarrow Fe_3O_4 + 4H_2O \tag{2.15}$$

In contrast to thermal decomposition, the co-precipitation method suffers from a poor separation of the nucleation and growth phases, resulting in a broader range of particle sizes and less uniformity of the final product. Despite the limitations in controlling the particle size distribution, co-precipitation remains a widely utilized method for synthesizing IONPs due to its simplicity, absence of the need for organic solvents, high yield, and cost-effectiveness [43].

2.2.4 Stabilization of Iron Oxide Nanoparticles

Bare IONPs dispersed in aqueous solutions exhibit weak colloidal stability, due to a combination of large interfacial energy and attractive forces such as van der Waals and magnetic interactions at close interparticle distances [44]. Aggregation can result in larger particle sizes and broader size distributions, which consequently can lead to loss of magnetism and dispersibility. Along with this, IONPs express a high degree of chemical reactivity. Under ambient conditions, magnetite nanoparticles tend to oxidize rapidly, which can alter their crystal structure and magnetic properties [45].

The susceptibility to aggregation and sensitivity to oxygen restrict the application of bare IONPs. To overcome these challenges, additional surface stabilization is necessary to preserve their stability and applicability. Moreover, stabilization and surface coatings can enhance biocompatibility and allow for tailored functionalization of the surface of IONPs [12]. In this context, the most widely adopted approach is to coat the IONPs with organic or inorganic substances [46]. Common organic materials include polymers such as dextran [47], chitosan [48] or polyethylene glycol

[49], as well as minor organic molecules such as amino acids [50], citric acid [51] or vitamins [52]. Silicates [53], carbon [54], metals such as gold [55] and silver [56], and metal oxides [57] are frequently used as inorganic coating compounds. Within this selection, silica coated IONPs have demonstrated excellent biocompatibility, hydrophilicity, and stability in aqueous solutions [53, 58].

2.3 Silica Coated Iron Oxide Nanoparticles

Silicon dioxide (SiO_2), known as silica, consists of silicon and oxygen, which are by far the two most dominant elements in the crust of the earth [59]. Silica is mainly found in nature as crystalline silica, which has been widely used throughout history for the production of glass, ceramics, and silicons, as well as a fundamental component in construction materials like concrete, mortar, and sandstone. In recent times, amorphous colloidal silica has been the subject of intense research and is one of the most employed nanomaterials [60]. The interest in colloidal silica as a nanomaterial stems from its advantageous properties, such as low toxicity, optical transparency, thermal stability, high colloidal stability in many conditions, easy surface functionalization, and excellent biocompatibility, which makes it especially ideal for biomedical applications. Furthermore, the use of silica as a coating material for different core materials, such as IONPs, has expanded the potential use of colloidal silica.

Although silica is easily accessible as a mineral, colloidal silica is generally synthesized through chemical synthetic pathways due to the toxicity of crystalline silica and the challenge of controlling size, shape, and impurity levels during the processing of naturally occurring silica [13]. A common way to synthesize colloidal silica is through the Stöber method (sol-gel based). This is a well-developed method that allows for the production of spherical and monodisperse silica nanoparticles with highly tailorable size and surface properties. The method has subsequently been developed as a common approach for coating IONPs with silica [46].

2.3.1 The Stöber Method

The Stöber method, developed by Stöber, Fink, and Bohn [61] in 1968, is a widely used technique for synthesizing colloidal silica nanoparticles through the hydrolysis and polycondensation of alkoxysilanes. Typically, tetraethyl orthosilicate (TEOS) is combined with a water-alcohol mixture in the presence of a base catalyst, such as an ammonia solution. The chemical reactions for the process are presented by Equations 2.16-2.18 [62]. Initially, TEOS is hydrolyzed into a silanol monomer by nucleophilic substitution of ethoxy groups (-OR) by hydroxyl groups (-OH) from the solvent. The rate of hydrolysis increases with ammonia concentration, as hydroxide ions from ammonia are more effective nucleophiles than water molecules. Furthermore, the rate of hydrolysis of a molecule expands as more ethoxy groups are converted to hydroxyl groups, as a result of an

increased positive charge on the silicon atom and a decrease in steric hindrance [62, 63].

$$\textbf{Hydrolysis: } Si(OR)_4 + xH_2O \overset{NH_3}{\rightleftharpoons} Si(OR)_{4-x}(OH)_x + xROH \tag{2.16}$$

$$\textbf{Water condensation: } 2Si(OR)_{4-x}(OH)_x \rightleftharpoons (RO)_{8-2x}(Si\text{-}O\text{-}Si)(OH)_{2x-2} + H_2O \tag{2.17}$$

$$\textbf{Alcohol condensation: } Si(OR)_4 + Si(OR)_{4-x}(OH)_x \rightleftharpoons (RO)_{7-x}(Si\text{-}O\text{-}Si)(OH)_{x-1} + ROH \tag{2.18}$$

Hydrolysis is subsequently followed by condensation to form siloxane bonds (*Si-O-Si*) which proceeds to the formation of a silica network. From Equation 2.17, either two silanol groups (*-Si-OH*) condense and release water, or from Equation 2.18, silanol groups and unhydrolyzed ethoxy groups condense and release alcohol. The siloxane clusters are subsequently connected via polycondensation, leading to the formation of initial nuclei, that grow further into colloidal silica nanoparticles [64]. Similarly to hydrolysis, condensation involves nucleophilic attachment, where silanol groups act as nucleophiles. The condensation rate is higher than the hydrolysis rate, considering the fact that silanol groups are deprotonated more easily than water, increasing the positive charge density of the silicon atom to a favorable nucleophilic attach. As such, silanol monomers attach more readily to larger siloxane networks than monomers or smaller oligomers [62, 63].

For the Stöber Method, two different growth models for colloidal silica particles are well accepted in the literature, namely the monomer addition model and the aggregation growth model [13]. The monomer addition model is originally based on the classical LaMer model provided by Lamer and Dinegar in 1950 [21]. This model describes nucleation as homogeneous, where stable nuclei burst out of the solution during a limited period of time once supersaturation is achieved. After nucleation, growth occurs by polycondensation of silanol monomers from the solution on the surface of the newly formed nuclei. In contrast, according to the growth aggregation model, growth occurs by the binary collision of nuclei, also referred to as primary particles or subparticles, until a stable colloidal particle size is reached [13, 65]. Other hypothesis suggest a combination of the two models, where aggregation occurs in the early stages of growth followed by growth based on monomer addition [13, 66]. Generally, research has demonstrated that both of the models can be supportive in explaining particle formation under various conditions. However, the complete growth mechanism of the Stöber method and its kinetics are not yet fully understood, which serves as a limitation for this approach [46].

Several modified Stöber methods have been developed for different applications. The process is frequently used for silica coating of metals and metal oxides such as gold nanoparticles [67] and

IONPs [1, 53]. Monolayers and multilayers of siloxanes can be grown on surfaces with accessible hydroxyl groups, a process defined as *silanization*. Silanization is a low-cost, simple, and effective procedure to modify a material surface with silica [68]. For the silanization of IONPs based on the Stöber method, typically prior synthesized IONPs are combined with a mixture of alkoxysilanes and water/alcohol, before the synthesis is initiated by adding ammonia as a catalytic base [1, 53]. Initially, as presented by Equation 2.16, alkoxy groups (*-Si-OR*) of the given silica precursor is hydrolyzed into silanol groups (*-Si-OH*). The condensation given by Equations 2.17 and 2.18 form siloxane bonds (*Si-O-Si*), which proceed to the formation of a silica network. Simultaneously, condensation occurs between silanol groups (*-Si-OH*) and hydroxyl groups (*-OH*) on the surface of IONPs, forming covalent iron-oxygen-silicon bonds (*Fe-O-Si*) [69]. Consequently, this links the IONPs to the silica network, allowing them to be effectively coated with a layer of silica.

2.3.2 Effect of Silanization Conditions on Particle Properties

The combination of the superparamagnetic property of IONPs and the colloidal stability and surface chemistry of silica results in unique characteristics for silica coated IONPs. However, a layer of silica increases the particle size and reduces the magnitude of saturation magnetization per unit mass, as silica is a non-magnetic material. Since several applications require particles with tiny dimensions and high magnetic saturations, it is important to understand how to control the thickness of the silica shell, final particle size, and morphologies by adjusting synthetic reaction conditions.

Recently, Ali *et. al* [1] reported a study of superparamagnetic silica coated IONPs by a modified Stöber method, where particle sizes and morphologies were tuned by controlling different reaction conditions. According to these findings, the choice of solvent had a significant impact on the actual size of the silica coated INOPs, with isopropanol producing larger sizes than ethanol. This phenomenon was explained by the higher polarity and dielectric constant of ethanol, which affect the hydrolysis rate and aggregation behavior. The strong hydrogen bonding between ethanol and hydroxyl groups slows down hydrolysis, resulting in smaller particle sizes. Additionally, the higher dielectric constant of ethanol creates stronger static repulsive forces, which inhibit the aggregation of larger particles to a greater extent.

In contrast to the majority of scientific literature, which typically reports only two morphologies (aggregated or spherical), the study of Ali *et. al* [1] uncovered four distinct morphologies: irregular, fused, aggregated, and spherical. The concentration of ammonia as a catalyst was found to have a significant influence on the morphology of the silica coated IONPs. Based on their research, it was hypothesized that at low ammonia concentrations (0.16 M), the hydrolysis of silanol monomers is limited, resulting in the formation of irregularly shaped particles. In contrast, silanol monomers synthesized at high ammonium hydroxide concentrations (> 0.62 M) get more hydrolyzed, leading to growth in a three-dimensional pattern into spherical-shaped silica coated IONPs.

In addition to the type of solvent and concentration of the catalyst, there are multiple other factors that may affect the silanization synthesis. For instance, the reaction time, concentration of IONPs, concentration of silica precursor, total solvent volume, functional groups on the surface of the IONPs, and the specific type of silica precursor employed, to mention a few. While TEOS is known for providing hydroxyl groups (*-OH*) on the surface of silica coated IONPs, alternative silica precursors, such as organofunctional alkoxysilanes, can also be utilized. This enables the incorporation of diverse functional groups onto the surface of silica coated IONPs. Consequently, organic silica functionalization creates many opportunities and may have a significant impact on the stability and applicability of the particles.

2.3.3 Organic Functionalization of Silica Coated Iron Oxide Nanoparticles

Organofunctional alkoxysilanes, also called silane coupling agents, are silanes with two reactive groups that can connect inorganic surfaces, like silica or IONPs, to organic materials. The general molecular structure of an organofunctional trialkoxysilane can be written as:

$$R' - (CH_2)_n - Si(OR)_3 \tag{2.19}$$

where *-OR* is an hydrolyzable alkoxy group, typically methoxy or ethoxy, while R' is a nonhydrolyzable organic group, such as amine [53], vinyl [70], mercapto [71], thiol [72] and others [73].

Generally, there are two approaches to achieving organic surface functionalization of silica coated IONPs via covalent bonding: post-synthetic grafting and co-condensation. Post-synthetic modification, which is the most common route, involves an additional synthetic step after the fundamental silica coating of IONPs. In this process, the exposed surface silanol groups of silica react with the silane coupling agents, resulting in the incorporation of the desired functional groups onto the surface. On the other hand, in the co-condensation approach, also referred to as a one-pot synthesis, organofunctional alkoxysilanes are directly combined with traditional tetraalkoxysilanes, such as TEOS. The alkoxy groups are hydrolyzed into silanol groups, which are then co-condensed to create a silica network between the various silane compounds. The latter approach is considered simpler because it only requires one step, and typically provides a more homogeneous distribution of functional groups [74, 75].

2.4 Amine-Functionalized Silica Coated Iron Oxide Nanoparticles

The work performed in this thesis, which focuses on amine-functionalized silica coating of IONPs, is greatly inspired by the research conducted by Digigow *et al.* [53]. Digigow *et al.* reported a modified Stöber method, combining tetraethyl orthosilicate (TEOS) and 3-aminopropyltriethoxysilane (APTES) in a co-condensation approach, to obtain amine-functionalized silica coated IONPs. Among various organofunctional alkoxysilanes, APTES is

commonly utilized for functionalizing oxide surfaces with primary amine groups (-NH_2) [76]. Amines are especially useful due to their diverse reactive pathways, and they frequently serve as reactive sites for the conjugation of biomolecules for specific applications [77]. Additionally, a monolayer of APTES on silica coated IONPs imparts a positive net charge and colloidal stability in aqueous solutions at physiological pH levels [78].

2.4.1 Effect of Silanization Conditions on Particle Properties

In the study conducted by Digigow *et al.* [53], superparagmagnetic IONPs were successfully coated with amine-functionalized silica, leading to particles with a multiple IONPs core - silica shell architecture. A combination of TEOS and APTES was employed as the silica precursors, since it was initially observed that silanization with only APTES resulted in virtually no silica coating on the IONPs surface. The research proposed that the observed morphology is primarily attributed to the presence of the aminopropyl group in APTES. It is known that trialkoxysilanes, such as APTES, typically show a lower level of cross-linking density in the silica network compared to tetraalkoxysilanes, such as TEOS [79]. According to Van Blaaderen *et al.* [80], APTES is prone to form six- or five-membered chelate rings in basic solutions, which sterically hinder the condensation of APTES to form precipitated particles by itself. Chen *et al.* [81] demonstrated the formation of a strong hydrogen bond between the amine group (-NH_3^+) on one APTES molecule and the silanol group (-*Si*-O^-) on another APTES molecule. It was proposed that if this interaction is sufficiently strong, it can disrupt the condensation process with other APTES molecules, and as a result, no particles will be formed. Chen *et al.* suggested that the morphology of amine-functionalized silica nanoparticles in a co-condensation approach is primarily governed by the hydrolysis and condensation of TEOS, as APTES alone does not result in silica precipitation.

Chen *et al.* [81] conducted a study specifically focusing on the role of APTES in the production of silica nanoparticles using a Stöber approach. A system consisting of TEOS, APTES, ethanol, and water, without the addition of ammonia as a basic catalyst was investigated. Interestingly, the precipitation of particles without adding ammonia solution demonstrated the self-catalytic effect of APTES, where APTES enables the hydrolysis and condensation of both silanes. Chen *et al.* further discovered that the content of APTES in the precursor mixture had a significant impact on the size and morphology of the particles. When the molar ratio of APTES/TEOS was low, typically 0.1, independent spherical particles with sizes ranging from 300 to 400 nm were obtained. In contrast, higher ratios of 1 and 2 resulted in spheres of 250 nm and 150 nm, respectively, that were highly agglomerated and fused. Consequently, the study revealed that as the APTES content in the precursor solution increased, the size of silica nanoparticles decreased while the degree of agglomeration increased.

Digigow *et al.* [53] studied the effects of varying the weight percentage of APTES in relation to the total mass of TEOS and APTES, and the mass ratio of IONPs to theoretically obtained silica

on the size and morphologies of the resulting silica coated IONPs. Increasing the mass of APTES from 0 wt% to 25 wt% resulted in smoother particles, with reduced anisotropy and slightly larger particle sizes. The hydrodynamic sizes were increased from approximately 70 nm to 180 nm from 0 wt% to 25 wt% APTES. On the other hand, increasing the silica mass while keeping the number of IONPs fixed resulted in particles with rougher surface textures, increased anisotropy, thinner silica shells, and a higher number of IONPs incorporated within the silica matrix. Additionally, the study revealed that the introduction of APTES caused an increase in the zeta potential of the silica coated IONPs. It is reported in the literature that silica surfaces of TEOS are negatively charged above its isoelectric point (pH >2), due to the presence of deprotonated silanol groups (SiO^-) [82]. The addition of APTES provides protonated amine groups (NH_4^+) in water, which consequently increases the zeta potential. However, the magnitude of the increase in the study of Digidow *et al.* was less remarkable at higher APTES concentrations, suggesting saturation of the surface with amine groups. Furthermore, by using Hermanson's colorimetric assay, Digidow *et al.* confirmed the presence of a greater number of protonated amine groups on the particle surface, as the concentration of ATPES was increased.

In the specialization project conducted in fall 2022, functionalized silica coated IONPs were produced in a similar manner as Digigow *et al.* [53], with variations in silanization parameters. Input reaction parameters, including the quantity of IONPs, the mass of silica precursor, and the type of IONPs synthesized by thermal decomposition and co-precipitation, were adjusted in the project. By increasing the precursor amount, is was obtained larger spherical particles with higher stability, as indicated by the zeta potential, but lower saturation magnetization values. The size and magnetic properties were also influenced by the mass of applied IONPs, with smaller particles and higher magnetization values observed for a larger quantity of IONPs. In the event of silica coated thermal decomposition IONPs, the particles were to a greater extent spherical and slightly smaller, but had a slightly lower saturation magnetization values compared to silica coated co-precipitation IONPs. It should be emphasized, that the presence of free amino groups on the particle surface was not confirmed in this study, but indicated by positive zeta potential measurements.

2.4.2 Quantification of Amine Groups

The presence and quantity of various functional groups on the surface of a designed nanomaterial have a significant impact on surface charge, and consequently on the colloidal stability and aggregation behavior of a nanoparticle. Additionally, surface chemistry plays a crucial role in determining the reactivity with other chemical species and its potential for further functionalization. Consequently, in order to control the performance of nanoparticles for specific applications, it is essential to characterize the surface chemistry accurately. In this context, there already exist several methods for identifying and quantifying functional groups, such as nuclear magnetic resonance (NMR), thermogravimetric analysis (TGA), X-ray photoelectron spectroscopy (XPS),

acid–base titrations, fluorescence, and colorimetric assays [83–87]. Among these, a number of studies have demonstrated that the colorimetric ninhydrin assay is a convenient and simple method for quantifying surface amine groups [84, 86, 87].

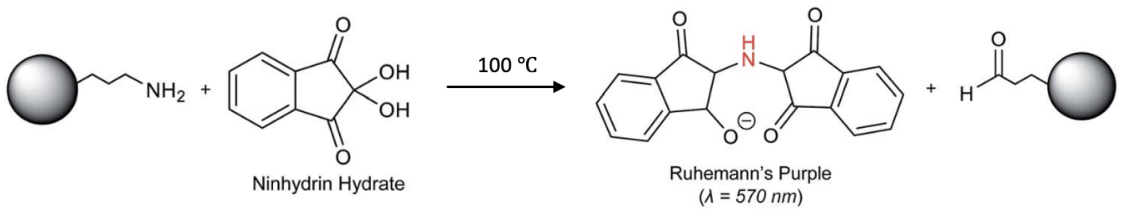

Figure 2.7: Reaction of a nanoparticle containing a primary amine group and a ninhydrin reagent into the Ruhemann's purple complex. The Figure is adopted from Sun *et. al* [86].

A colormetric ninhydrin assay inspired by the research of Karade *et. al* [87] and Sun *et. al* [86] was developed in this thesis. The assay is commonly used to detect and quantify amino acids and primary amine groups in solution. From Figure 2.7, the ninhydrin reagent in presence of primary amine groups, generates a purple colored complex named Ruhemann's purple, which consist of two ninhydrin-hydrates connected together by an imine bond. In accordance with Beer-Lamberts Law, the concentration of bound amines is directly proportional to the absorption of the dye, which is measured by UV-visible spectroscopy (UV-vis) at 570 nm [86, 87].

In general, scientific literature presents a wide range of different conditions for the ninhydrin assay, such as reaction time, solvent, temperature and amine standards. In a previous study by Sun *et al.* [86], both octylamine, leucine, and APTES, were used to calibrate the product yield from a ninhydrin assay. The findings revealed that APTES has a tendency to undergo polymerization, resulting in variable and diminished curves. Since leucine is an amino acid, it was found that octylamine, which is a stable and non-volatile primary amine, served as a better model for the calibration of primary amine groups on nanoparticles. Consequently, it is essential to select the optimal reaction conditions for the ninhydrin assay in order to obtain optimal signals and reliable data.

Chapter 3

Methodology

This chapter provides an overview of the experimental work conducted in this thesis, focusing on the detailed procedures for the synthesis and characterization of the particles. It should be noted that parts of this chapter are adopted from previous work.

3.1 Materials

Table 3.1: An overview of all the chemical used with purity and manufacturer.

Chemical	Purity	Manufacturer
Ethanol absolute	100%	VWR Avantor
Ammonia solution (NH_4OH)	25%	Sigma-Aldrich
Ethyl acetate	$\geq$ 99.5%	Sigma-Aldrich
Iron(III) acetylacetonate ($Fe(acac)_3$)	$\geq$ 97.0%	Sigma-Aldrich
Tri(ethylene glycol) (TREG)	$\geq$ 99.0%	Sigma-Aldrich
Tetraethyl ortosilicate (TEOS)	$\geq$ 99.0%	Sigma-Aldrich
3-Aminopropyl triethoxysilane (APTES)	99%	Sigma-Aldrich
Octylamine	99%	Sigma-Aldrich
Sodium hydroxide (NaOH) (pellets)	99.0%	Sigma-Aldrich
Hydrochloric acid (HCl)	37%	VWR Avantor
Sodium chloride (NaCl)	$\geq$ 99.9%	VWR Avantor
Ninhydrin	99%	Sigma-Aldrich
Argon gas	$\geq$ 99.9%	AGA AS

The chemicals used in this thesis with the associated purity grade and manufacturer are presented in Table 3.1. Distilled deionized water (MQ-water) was provided by Sartorius Arium water purification systems (18.2 MΩcm c). Some of the chemicals were further prepared and diluted, which

is highlighted in the following sections.

3.2 Synthesis of Iron Oxide Nanoparticles by Thermal Decomposition

Iron oxide nanoparticles (IONPs) were synthesized by thermal decomposition using a protocol based on the research of Maity *et al.* [40]. The setup is seen in Figure 3.1. Initially, 0.71 g of $Fe(acac)_3$ (2 mmol) was combined with 20 mL of TREG in a 100 mL three-necked round bottom flask equipped by a heater element. The flask had three necks, one connected to a thermometer, another to a reflux condenser filled with inert argon gas, and the last to an argon-filled balloon to prevent oxygen leakage in case of overpressure. The mixture of $Fe(acac)_3$ and TREG was magnetically stirred at 400 rpm and purged with argon gas for 5 min. The stirring speed of 400 rpm was maintained throughout the heating process. After purging with argon, the temperature was raised from room temperature to 120^oC at a rate of 20^oC per min. Once the temperature reached 120^oC, it was maintained for 1 hour before further heating to 280^oC at the same rate of 20^oC per min. The system was held at 280^oC for 2 hours. Subsequently, the flask was removed from the heater and allowed to cool down to 25^oC at room temperature. The solution was then transferred to two 50 mL centrifuge tubes, with 10 mL of solution added to each tube. To precipitate the IONPs, 20 mL of ethyl acetate was added to each tube. The nanoparticles were separated from the solution using a magnet, and the supernatant was removed. The particles were washed three times by dispersing them in 10 mL of ethanol, mixing with vortex for 20 sec, adding 20 mL of ethyl acetate, mixing with vortex for 20 sec, and then separating them with a magnet for 30 sec to 1 min. Finally, the particles were collected in one centrifuge tube with 20 mL of MQ-water and stored at 4^oC.

Figure 3.1: Setup for Thermal Decomposition of IONPs.

It should be noted that the increased temperature rates and dwelling times were automatically set by a built-in program provided by the heating element. For the two raised temperature steps, the heating rate was set to 20^oC per min, while the real heating rate measured by the thermometer was slower. This indicates that the system was heated at the maximum feasible rate. At each of these stages, the program was temporarily paused when the program reached the set temperatures of 120^oC and 180^oC, respectively, and it resumed running once the thermometer reached these set temperatures.

3.3 Synthesis of Amine-Functionalized Silica Coated Iron Oxide Nanoparticles

The experimental design presented in Table 3.2 was utilized for the silanization experiments. Parameters that were varied were: the solvent volume, the weight percentage of APTES of the total TEOS and APTES amount, and the type of IONPs. The silanization procedure is highly inspired by the study of Digigow *et al.* [53].

Figure 3.2: Setup for the silanization reaction.

Typically, 80 mL of ethanol was added to a 250 mL conical flask, followed by magnetic agitation at 300 rpm, which was maintained throughout the entire reaction. Figure 3.2 depicts the setup of the conical flask with ethanol and the magnet. The flask was positioned on a combined heating and stirring plate, but the reaction itself took place at room temperature without any additional heating. 140 μL of TEOS, followed directly by 46 μL of APTES, was added to the solution of ethanol. After 10 min, a pre-prepared solution of 10 mg IONPs in 20 mL of MQ-water was added into the ethanolic solution. This IONPs in MQ-water solution was in advance solution mixed by vortex

Table 3.2: The reaction parameters varied for the full factorial design.

Experiment Name	Solvent Amount [mL]	APTES Amount [wt%])	IONPs [Synthesis Type]
S20-5%-TD	20	5	Thermal Decomposition
S20-15%-TD	20	15	Thermal Decomposition
S20-25%-TD	20	25	Thermal Decomposition
S50-5%-TD	50	5	Thermal Decomposition
S50-15%-TD	50	15	Thermal Decomposition
S50-25%-TD	50	25	Thermal Decomposition
S60-15%-TD	60	15	Thermal Decomposition
S100-5%-TD	100	5	Thermal Decomposition
S100-15%-TD	100	15	Thermal Decomposition
S100-25%-TD	100	25	Thermal Decomposition
S20-5%-CP	20	5	Co-Precipitation
S20-15%-CP	20	15	Co-Precipitation
S20-25%-CP	20	25	Co-Precipitation
S50-5%-CP	50	5	Co-Precipitation
S50-15%-CP	50	15	Co-Precipitation
S50-25%-CP	50	25	Co-Precipitation
S60-15%-CP	60	15	Co-Precipitation
S100-5%-CP	100	5	Co-Precipitation
S100-15%-CP	100	15	Co-Precipitation
S100-25%-CP	100	25	Co-Precipitation
S100-100%-TD	100	100	Thermal Decomposition
S100-100%-CP	100	100	Co-Precipitation
S100-0%-TD	100	0	Thermal Decomposition
S100-0%-CP	100	0	Co-Precipitation

and placed in an ultrasonic bath (vortex 1 min + sonication 8 min + vortex 1 min). Following an additional 5 min, 1 mL of the ammonia solution was introduced to the mixture. The reaction was allowed to proceed for 3 hours before the content was transferred to four 50 mL centrifuge tubes. The particles were separated by centrifugation at 14500 rpm for 20 min. The supernatant was discarded, and the particles were combined in one tube and subjected to five cleaning cycles. Each cleaning cycle involved dispersing the particles in 10 mL of MQ-water, vortexing for 30 sec, sonication for 8 min, vortexing for another 30 sec, and then centrifuging at 14500 rpm for 15 min. Finally, the silica-coated IONPs were stored in 10 mL of MQ-water at 4°C.

It should be highlighted that the approach described above is a general procedure, and the size

of the conical flask, the quantities of ethanol, water, APTES, TEOS, and ammonia used in each experiment in this study were all different. A detailed summary of the specific conditions and quantities of chemicals employed in each experiment can be found in Appendix A, Table A.1. Furthermore, it should be noted that the reaction conditions of preliminary experiments are pointed out in the result and discussion section and not included in Table A.1.

3.4 Ninhydrin Assay

The ninhydrin assay was used for the quantification of amine groups on the surface of the silica coated IONPs. The assay was developed during this research, and the procedure is strongly inspired by the study of Sun *et al.* [86] and Karade *et al.* [87]. A calibration curve of at least five points was prepared the same day, before the analysis with nanoparticles.

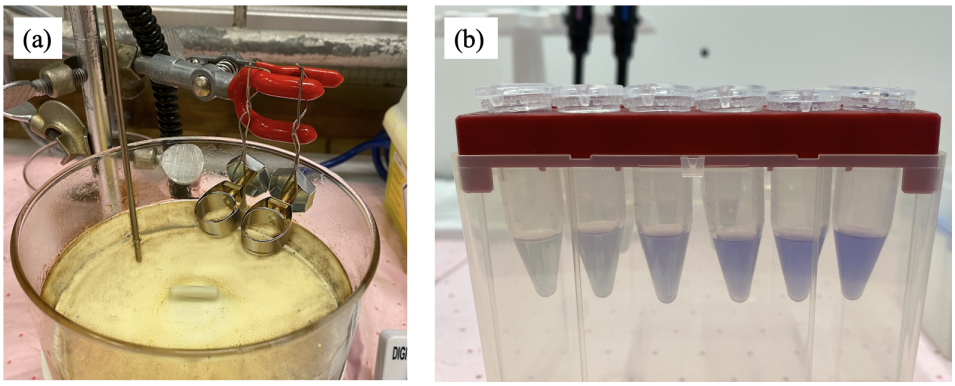

Figure 3.3: Image (a) shows the reaction setup for the ninhydrin assay, while image (b) illustrates the final reacted samples used to construct the calibration curve.

Baseline

Initially, a baseline solution was prepared by mixing 750 μL ethanol + 250 μL MQ-water in an eppendorf tube. A minimum of 600 μL of baseline solution was transferred to a 500 μL quartz cuvette and the absorbance spectrum was measured by ultraviolet–visible spectroscopy (UV-vis). It should be noted that the UV-vis light interacted with the sample specifically at the 500 μL mark of the cuvette, and therefore a larger volume was added to ensure proper interaction. This absorbance measurement was used as a reference and automatically subtracted from all the subsequent measurements by the Cary WinUV Software connected to the UV-vis instrument.

Calibration Curve

A calibration curve was prepared using octylamine as the amine-containing specie. A stock solution of 1 mg/mL octylamine in a mixture of 50% ethanol and 50% MQ-water was created. This

stock solution was then serially diluted in eppendof tubes to obtain a variety of concentration points, typically ranging from 0.160 mg/mL - 0.062 mg/mL. A ninhydrin solution was prepared by dissolving ninhydrin crystals in ethanol at a concentration of 20 mg/mL (corresponding to 2% ninhydrin solution). The solution was kept in an ultrasonic bath and mixed well by vortex until all the ninhydrin crystals were dissolved. For each of the different octylamine concentration points, 500 μL of the octylamine solution and 500 μL of ninhydrin solution were transferred to a 5 mL eppendorf tube, as depicted in Figure 3.3 image (b). The eppendorf tube was immediately mixed by vortex for 30 sec and kept in an ultrasonic bath for 1 min, before it was placed in a holder in a preheated oil bath set at 100 ^{o}C. The holders in the oil bath refer to the metal fastenings depicted in Figure 3.3 image (a). They were placed such that the tip of the eppendorf tube with solution was completely covered of oil. After 10 min, the eppendorf tube was removed from the oil bath and moved to the freezer, where it was kept for 2 min. Thereafter, a minimum of 600 μL of the solution was transferred to a 500 μL quartz cuvette. Subsequently, the absorbance of the solution was measured by UV-vis. The entire absorbance spectrum ranging from 200 - 1000 nm was obtained, while the data point at 570 nm was specifically used further.

Subsequently, the calibration curve was developed by plotting the absorbance at 570 nm on the y-axis to the corresponding known measured concentration of octylamine on the x-axis. It should be highlighted that the different concentrations of octylamine solution and the ninhydrin solution were prepared simultaneously. However, once the octylamine solution was mixed with the ninhydrin solution, the procedure was carried out for a single sample without time delay.

Nanoparticle Measurements

Initially, diluted samples of silica coated IONPs were centrifuged in 1.5 mL eppendorf tubes until complete separation, before the supernatant was removed and replaced with 50% ethanol and 50% MQ-water. The dilution of the sample was adjusted in accordance with the subsequent absorbance measurement, to ensure that the measurement was in the range of the calibration curve. Typically, sample S100-25%-TD was diluted to a concentration of 0.4 mg/mL, which corresponded to an absorbance of 0.4. The ninhydrin solution was prepared by dissolving ninhydrin crystals in ethanol at a concentration of 20 mg/mL (corresponding to 2% ninhydrin solution). The solution was kept in an ultrasonic bath and mixed well by vortex until all the ninhydrin crystals were dissolved. For each of the different measurements, 500 μL of the diluted particle solution and 500 μL of ninhydrin solution were transferred to a 5 mL eppendorf tube. The eppendorf tube was mixed by vortex for 30 sec and kept in an ultrasonic bath for 1 min, before it was placed in a holder in a preheated oil bath set at 100 ^{o}C. They were placed such that the tip of the eppendorf tube with solution was completely covered of oil. After 10 min, the eppendorf tube was removed from the oil bath and moved to the freezer, where it was kept for 1 min. Afterwards, the entire solution was transferred to a 1.5 mL eppendorf tube, which was centrifuged at 14 500 rpm for a minimum of 3 min, until

the nanoparticles were cleary separated from the colored solution. Thereafter, a minimum of 600 μL of the supernatant was carefully transferred to a 500 μL quartz cuvette. Subsequently, the absorbance of the solution was measured by UV-vis. The entire absorbance spectrum ranging from 200 - 1000 nm was obtained, while the data point at 570 nm was specifically used further.

The concentration of amine groups in the sample was determined by comparing the absorbance at 570 nm to the obtained absorbance value in the calibration curve. It should be highlighted that the different concentrations of nanoparticles and the ninhydrin solution were prepared simultaneously and eventually. However, once the nanoparticle solution was mixed with the ninhydrin solution, the procedure was carried out for a single sample without time delay.

3.5 Magnetic Separation Experiments

There were performed some experiments where the solution pH of the silica coated IONPs was varied, while the hydrodynamic sizes, zeta potentials and magnetic separation times were measured. This section explains the sample preparation procedures of these experiments.

Hydrodynamic Sizes and Zeta Potentials

The samples were prepared by taking out a small volume of nanoparticles dispersed in water and further diluting it with MQ-water to a volume of approximately 6 mL. The dilutions were done to achieve a final transmittance percentage of dynamic light scattering (DLS) within the range of 40-50%. The diluted samples was separated equally into two glass vials. In one vial, the pH was raised by adding drops of diluted NaOH, while in the other vial, the pH was lowered by adding diluted HCl. The pH of the solution was measured using a pH meter equipped with a semi-micro pH probe. During the measurement, the solution was continuously stirred using a magnetic stirrer. The hydrodynamic sizes and zeta potentials were then measured by Anton Paar LiteSizer 500 at different pH levels.

Magnetic Separation Times

For the variation of pH, samples were prepared by transferring nanoparticles dispersed in water into two glass vials, with a volume of 5 mL in each. In one vial, the pH was raised by adding drops of diluted NaOH, while in the other vial, the pH was lowered by adding diluted HCl.

For experiments of nanoparticles dispersed in NaCl, samples were prepared by centrifuging 5 mL of nanoparticles suspension until complete separation. The supernatant was discharged and replaced with NaCl solution and transferred to a glass vial. The NaCl crystals were dissolved in MQ-water in advance to solutions of concentrations of 0.1 M and 1.0 M.

The pH of all the samples was measured using a pH meter equipped with a semi-micro pH probe.

During the measurement, the solution was continuously stirred using a magnetic stirrer. The magnetic separation times were measured at the different pH levels and NaCl concentrations. The sample in the glass vial was mixed properly by vortex for 20 sec. Subsequently, it was placed close to a magnet and the time was recorded until the nanoparticles were visually separated from the solution. These separations were captured using an iPhone to ensure consistency in the visual appearance of the separation endpoint.

3.6 Characterization Instruments

The synthesized particles were characterized by using various of instruments, including dynamic light scattering (DLS), scanning transmission electron microscopy (STEM) with energy dispersive X-ray spectroscopy (EDS), vibration sample magnetometer (VSM) and ultraviolet–visible spectroscopy (UV-vis). The following sections provide a description of the sample preparation procedures associated with the instruments used in this study.

3.6.1 Dynamic Light Scattering

Anton Paar LiteSizer 500, which uses dynamic light scattering (DLS) technology, was utilized to measure the hydrodynamic diameters and zeta potentials of the synthesized particles. Samples were prepared by taking out a small volume of nanoparticles dispersed in water and further diluting it with MQ-water to a volume of 1 mL. The dilutions were done to achieve a final transmittance percentage within the range of 40-50%. The bare thermal decomposition IONPs were typically diluted at a ratio of 1:20 or more, while the silica-coated IONPs were diluted at ratios ranging from 1:10 to 1:2, depending on the initial concentration. After dilution, the solution was mixed by vortex for 30 sec and kept in an ultrasonic bath for 1 min, repeated three times. The solution was transferred to an omega cuvette, and the hydrodynamic sizes and zeta potentials were measured using the Anton Paar LiteSizer 500. Unless otherwise is stated in the result and discussion section, the measurements were conducted using the automatic settings of the software. The automatic mode involves runs of 10 sec for a measurement, for a total of three subsequent measurements. The software allows for a maximum of 60 runs per measurement, but it automatically stops a measurement once a sufficient amount of data has been collected. For bare IONPs, 'Magnetite' was selected as a material, while 'Silica amorph' was chosen for the silica coated IONPs.

3.6.2 UV-Vis Spectroscopy

Agilent Cary 60 Ultraviolet-Visible Spectrophotometer (UV-vis) was utilized in conjunction with the ninhydrin assay. In this case, the UV-vis measured the intensity of light absorbed by different concentrations of a chemical complex named Ruhemann's purple. A 500 μL quartz cuvette was used for all the measurements in this work, and the sample preparation is explained along with the

procedure of the ninhydrin assay in Section 3.4.

3.6.3 Scanning Transmission Electron Microscopy

The Hitachi High-Tech SU9000 scanning transmission electron microscopy (STEM), located at the cleanroom facilities of NTNU was utilized for capturing images of the particles obtained in this research. The connected energy dispersive X-ray spectroscopy (EDS) allowed for chemical elemental mapping. Samples were prepared by taking out a small volume of nanoparticles dispersed in water and further diluting it with MQ-water to a volume of 1 mL. Typically, bare IONPs were diluted at a ratio of 1:25 or more, while silica coated IONPs were diluted at ratios ranging from 1:10 to undiluted, depending on their initial concentrations. After dilution, the solution was kept in an ultrasonic bath for a minimum of 5 min and mixed by vortex for 30 sec. Subsequently, small droplets of the solution were applied onto a copper grid. The copper grid was held by a tweezer, such as the copper grid was exposed to only air. Droplets of the solution were added to the grid until the entire surface was covered, which caused the formation of a slight bubble that eventually burst. The excess solution was gently soaked up by pointing a moistened soft tissue paper along the edge of the grid after 30 sec. Thereafter it was left to dry for another 4 min until all the solution was evaporated. At the cleanroom facilities of NTNU, the copper grid was placed in the STEM holder and inserted into the chamber for measurements. The acceleration voltage and current were typically 20 kV and 10 - 15 μA, respectively. The STEM images were analyzed by ImageJ, which is a software specifically designed for size and shape analysis of images.

3.6.4 Vibration Sample Magnetometer

A Princeton Micromag 3900 Series vibration sample magnetometer (VSM) was used for measuring the magnetic properties. For the sample preparation, a volume of particle solution was transferred to glass vials and dried in an oven at 65°C for a minimum of 48 hours. Subsequently, 7-10 mg of the dried particles were added to a VSM capsule. The sample was placed in a sample holder which was vibrated perpendicular to a magnetizing field. The position of the sample holder was adjusted according to the calibration position of the instrument to ensure reliable measurements. The measurements were normalized by mass, and the slopes were corrected to account for paramagnetism above 70% of saturation.

Chapter 4

Results and Discussion

The characterization of synthesized iron oxide nanoparticles (IONPs) and silica coated IONPs are presented in this chapter. The outcomes of the experimental design presented in Section 3.3 are discussed with an emphasis on morphologies and particle sizes, as well as surface properties and magnetic responses. Scanning transmission electron microscopy (STEM) and energy dispersive X-ray spectroscopy (EDS) were used to assess the particle sizes, silica shell thicknesses, and morphologies, while dynamic light scattering (DLS) was employed to measure the hydrodynamic sizes and zeta potentials. The magnetic properties were examined by a vibrating sample magnetometer (VSM), and the number of amine groups on the particle surfaces was determined using a ninhydrin assay in combination with an ultraviolet-visible spectrophotometer (UV-vis).

4.1 Characterization of Iron Oxide Nanoparticles

IONPs were synthesized by thermal decomposition in accordance with the procedure given in Section 3.2. Co-supervisor, Zeeshan Ali, synthesized citrate coate IONPs by the co-precipitation method. The two types of IONPs, synthesized by thermal decomposition or co-precipitation with citrate coating are referred to as TD-IONPs and CP-IONPs, respectively. The objective was to coat these particles with silica, resulting in the formation of silica coated IONPs, which are discussed further in the following sections.

Particle Sizes

Figure 4.1 presents bright-field TEM images of spherical (a) TD-IONPs and (b) CP-IONPs, respectively. Figure 4.2 shows histograms of the particle size distributions of (a) TD-IONPs and (b) CP-IONPs. These distributions were obtained by analyzing bright-field TEM images in the software ImageJ, where the diameters of 500 randomly selected particles were measured for each of the IONPs types. Based on the obtained size distributions, the mean particle diameters with

standard deviations were obtained to be 8±1 nm for TD-IONPs and 1±3 nm for CP-IONPs. In contrast to the TEM size, DLS analysis provided the average hydrodynamic diameters with standard deviations to be 192±11 nm for TD-IONPs and 168±2 nm for CP-IONPs.

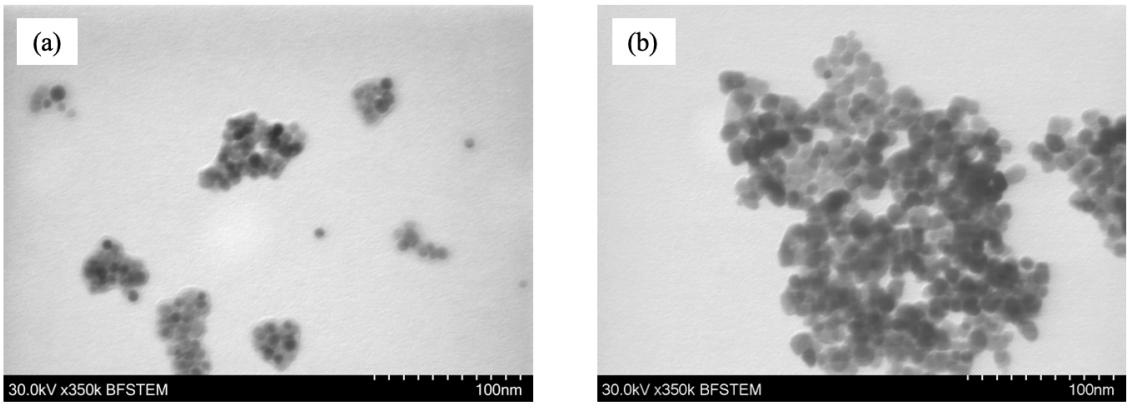

Figure 4.1: Bright-field TEM images of IONPs synthesized by (a) thermal decomposition and (b) co-precipitation method.

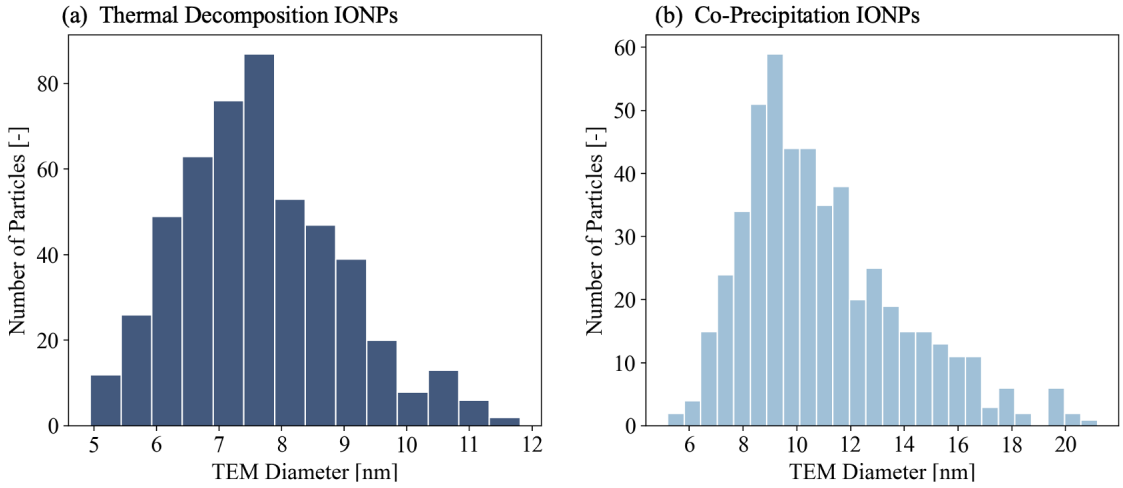

Figure 4.2: Particle size distribution of IONPs synthesized by (a) thermal decomposition and (b) co-precipitation method.

As discussed in Section 2.1.5, particles that move within a solution are constantly surrounded by a thin electric dipole layer. The hydrodynamic diameter of a particle refers to the diameter inclusive of this hydrated electrical layer. As a result, the hydrodynamic diameters are expected to be greater than the diameters measured from bright-field TEM images, which depict the particles in a dry state. The measured hydrodynamic diameters were observed to be approximately 15-25 times larger than the dry diameter of a single IONP. Prior to DLS measurements and STEM sample preparation, the samples were mixed by vortex and kept in an ultrasonic bath to prevent aggregation. However, the significantly larger hydrodynamic sizes compared to the dry sizes

indicate that the IONPs most likely aggregated during the DLS measurements. This is also evident in TEM images, as depicted in Figure 4.1, where the majority of particles appear to be aggregated, and only a few individual particles are observed.

Generally, as stated in Section 2.2.2 and 2.2.3, synthesis of IONPs by thermal decomposition is expected to generate monodisperse particles due to the effective separation of the nucleation and growth phases, whereas synthesis by co-precipitation offers limited control over particle size. This is apparent from the histograms shown in Figure 4.2. The size distribution of CP-IONPs is broader, ranging from approximately 5 nm to 21 nm, compared to TD-IONPs, where the sizes vary from 5 nm to 12 nm. Consequently, these results show that the TD-IONPs synthesized by thermal decomposition exhibited smaller particle sizes and a more uniform distribution, compared to the CP-IONPs synthesized by co-precipitation.

Surface Properties

The measured mean zeta potentials with standard deviations for TD-IONPs and CP-IONPs dispersed in water were found to be 33.2±0.2 mV and -38.05±0.6 mV, respectively. In aqueous solutions, bare IONPs generally form surface hydroxyl groups that are charged by protonation or deprotonation, depending on the pH of the system. The isoelectric point for bare IONPs is typically observed around pH 6.8, which makes them unstable in water and at physiological pH levels [43].

The positive zeta potential value observed for TD-IONPs can be explained by the presence of triethylene glycol (TREG) on the particle surfaces. According to Maity *et al.* [40], TREG molecules are polarized into $R\text{-}O^-$ and H^+ at elevated reaction temperatures. The $R\text{-}O^-$ component coordinates with Fe^{2+}/Fe^{3+} ions and the H^+ ions are attached at the surface, causing positively charged particles. The CP-IONPs, on the other hand, were coated with citrate ions, which provide negative electrostatic stabilization. Consequently, the zeta potential measurement for CP-IONPs was negative.

Magnetic Properties

The magnetization curves for TD-IONPs and CP-IONPs were measured by VSM and are displayed in Figure 4.3. The TD-IONPs and CP-IONPs had similar magnetization saturation values of 57.05 emu/g and 52.08 emu/g, respectively. Both curves show no hysteresis loop and display zero coercivity. The detection of sufficiently small particle sizes from the TEM images, suggests that the IONPs can be classified as single domain particles. In accordance with the magnetization curve, this indicates that the synthesized TD-IONPs and CP-IONPs were superparamagnetic. Moreover, Maity *et al.* [40] reported their synthesized TD-IONPs to have a magnetic saturation value of 65 emu/g. The lower value observed in this study could be due to the presence of a higher

fraction of non-magnetic TREG molecules attached to the surface of the TD-IONPs, which were not removed during the cleaning stages.

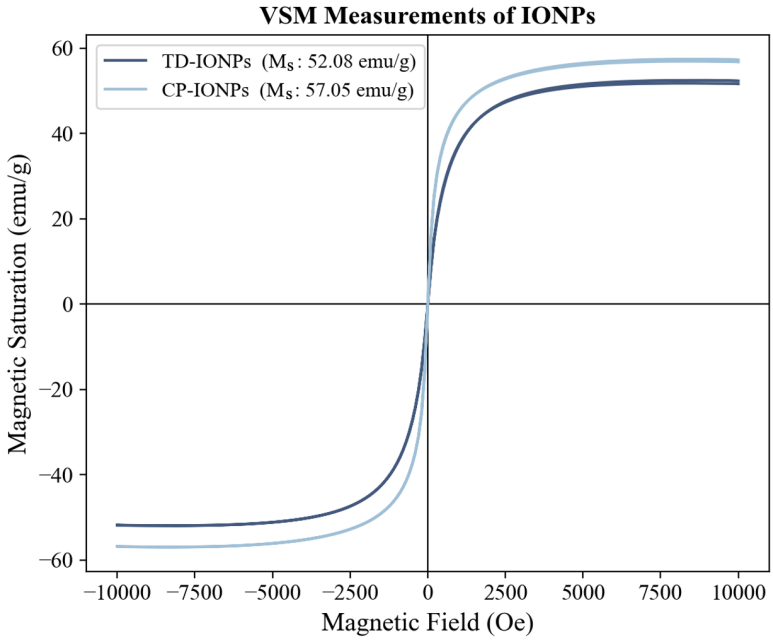

Figure 4.3: VSM measurements of IONPs synthesized by thermal decomposition and co-precipitation method

4.2 Preliminary Experiments

The TD-IONPs and CP-IONPs described in Section 4.1, were coated with silica according to the procedure given in Section 3.3. Based on the findings in the specialization project, written in the fall 2022 by the same author, preliminary experiments were conducted to fix certain silanization parameters and to determine which silanization parameters to investigate.

4.2.1 Varied Quantity of Iron Oxide Nanoparticles

In the specialization project, it was found that the saturation magnetization values were approximately three to five times larger when the quantity of IONPs added in synthesis was increased from 1.46 mg to 5.00 mg while all other synthesis parameters remained unchanged. It is desired to obtain a thin coating of silica in addition to particles with a high magnetization value, which rapidly separate in the presence of a magnetic field. Accordingly, some preliminary experiments were conducted to fix the ratio of theoretically obtained silica coating to the quantity of IONPs coated. In these experiments, the amount of TD-IONPs was varied, where 5 mg, 10 mg, and 25 mg of IONPs were added in the synthesis, while the amount of added silica precursors and other reaction parameters remained constant according to the general procedure given in Section 3.3.

Particle Sizes, Silica Shell Thicknesses and Morphologies

Figure 4.4 shows bright-field TEM images of samples from the different experiments, where the amount of TD-IONPs applied for silica coating is increased from left to right, with (a) 5 mg, (b) 10 mg and (c) 25 mg TD-IONPs. The particles consist of TD-IONPs, represented by the darker-colored cores, which are surrounded by a layer of silica. This observation is supported by EDS analysis, which will be discussed further in Section 4.3.3.

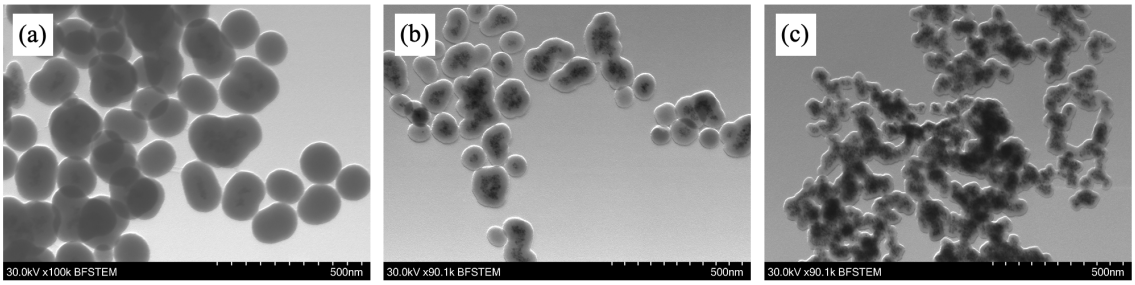

Figure 4.4: Bright-field TEM images of silica coated TD-IONPs were the amount of TD-IONPs utilized during the synthesis is varied: (a) 5 mg, (b) 10 mg, and (c) 25 mg TD-IONPs.

To determine the thickness of the silica shell, the distance between the outer dark IONPs core and the exterior silica surface of the particles was measured. Bright-field TEM images were analyzed using the software ImageJ, and a total of 200 random silica shells were examined for each experiment. It was observed that the mean silica shell thicknesses with standard deviations decreased from 51±4 nm to 31±3 nm to 14±2 nm, when the quantity of TD-IONPs was increased from 5 mg to 10 mg to 25 mg, respectively. This trend is also visible from the images in Figure 4.4, where the core become easier to observe as the number of TD-IONPs is increased. Moreover, it is apparent from the images that in the cases where 5 mg and 10 mg TD-IONPs were applied, spherical particles are observed, whereas when 25 mg TD-IONPs were applied, individual particles were not observed, but larger clusters of TD-IONPs with a thin silica coating. Based on this observation, the analysis of the dry diameters was only conducted for the experiments involving 5 mg and 10 mg IONPs. The mean dry diameters with standard deviations of 100 randomly selected particles were determined to be 126±11 nm in the event of 5 mg IONPs applied, and 100±21 nm when 10 mg IONPs were used in the experiment.

Digigow *et al.* [53] also conducted a study on the ratio of IONPs to silica. However, their approach involved keeping the quantity of IONPs constant while varying the concentrations of silica precursor. The observations made in this study are consistent with the findings of Digigow *et al.* [53]. They reported similar trends, noting that as the amount of silica added in relation to the IONPs decreased, the silica shell became thinner, the particle size decreased, the anisotropy increased, the surface became rougher, and a greater number of IONPs were incorporated into the silica shell. Based on the bright-field TEM images in Figure 4.4, it is evident that the IONPs

initially aggregate, as they are concentrated as a core and not evenly distributed in the silica matrix. According to the observations of Digigow *et al.*, 3-aminopropyl triethoxysilane (APTES) may prevent the aggregation of primary particles. Therefore, the increase in IONPs incorporation may be a result of the decrease in APTES in relation to IONPs, as APTES potentially hamper the initial formation of IONP aggregates. As proposed by Digigow *et al.*, the reason behind the poor particle morphology observed in the experiment where 25 mg of IONPs was applied, could be attributed to the relatively low quantity of silica compared to IONPs, which may not be enough to form and stabilize individual core-shell nanoparticles.

Magnetic Properties

The magnetization curves for the preliminary experiments were measured by VSM and are presented in Figure 4.5. The absence of a hysteresis loop and zero coercivity confirms the superparamagnetic property of the silica coated TD-IONPs. The magnetization saturations was increased from 5.30 emu/g to 13.71 emu/g to 19.36 emu/g, when the quantity of TD-IONPs utilized in the synthesis was increased from 5 mg to 10 mg to 25 mg, respectively.

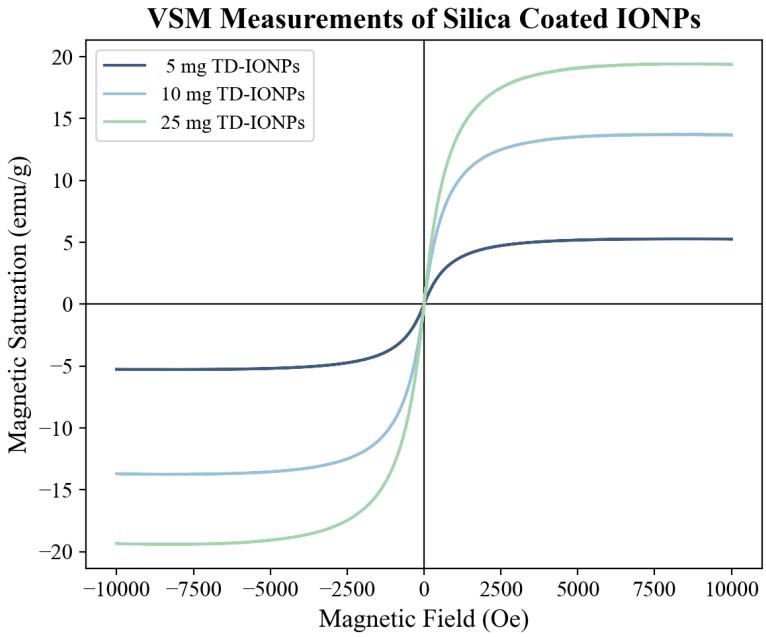

Figure 4.5: VSM measurements of silica coated TD-IONPs where the amount of TD-IONPs utilized during the synthesis is varied.

The magnetic behavior of silica-coated IONPs is only provided by the IONPs, while the magnetization saturation value is normalized by the total particle mass. Ideally, if the magnetic core is kept constant, a thicker non-magnetic silica shell will decrease the magnetic behavior of the silica-coated IONPs due to an increase in the total particle mass. Consequently, the increase in magnet-

ization saturation for these experiments as the quantity of TD-IONPs applied was increased, is as expected and it appears to be related to a combination of the decrease in silica shell thickness and the increase in the incorporation of IONPs, as observed in Figure 4.4. These findings are in agreement with the study of Digigow *et al.* [53], which also observed that the saturation magnetization increased with increasing IONPs to silica ratio.

In many applications, the aim is to obtain particles with high magnetization. However, considering that it is also desired to create individual particles of small sizes, adding 10 mg IONPs while keeping the quantity of silica constant, appears to be the most optimal choice based on these experiments. As a result, the IONPs to silica ratio was fixed in the subsequent experiments, with 10 mg IONPs combined with a theoretically determined quantity of 49 mg silica.

4.2.2 Varied Total Volume of Solvent

The amount of solvent utilized in the general silanization procedure given in Section 3.3, which was developed during the specialization project, is significantly more than the amount used in comparable procedures. For instance, in the specialization project, a total volume of 100 mL solvent was used, yielding dry particle sizes in the range of 100-300 nm, whereas in the protocol applied in the work of Ali [1], only 20 mL solvent was used, yielding dry particle sizes in the range of approximately 600-900 nm. This raises the question of whether a large volume of solvent may have a significant impact on particle properties. Consequently, some preliminary experiments were performed to determine which distinct solvent volumes to investigate for an experimental design in this research. Three experiments were carried out, with 50 mL, 100 mL, and 150 mL of solvent investigated, while TD-IONPs were applied and all reaction parameters were kept constant according to the general procedure in Section 3.3. It should be noted that the varied total volume of solvent is referred to as the combination of ethanol and MQ-water, varied in a constant ratio.

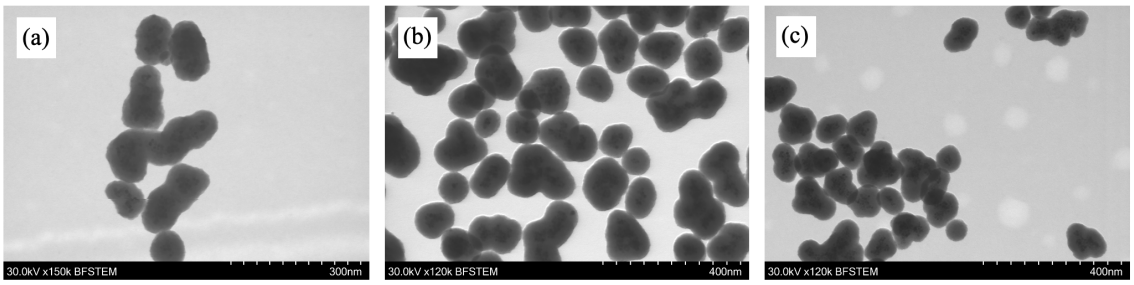

Figure 4.6: Bright-field TEM images of silica coated TD-IONPs were the total solvent amount in the synthesis is varied: (a) 50 mL, (b) 100 mL, and (c) 150 mL.

Figure 4.6 depicts the obtained bright-field TEM images of the silica coated TD-IONPs produced where (a) 50 mL, (b) 100 mL and (c) 150 mL solvent volumes were applied in the synthesis. It was difficult to observe any reliable and significant distinctions in size and morphologies based on the

bright-field TEM images. Consequently, the samples were analyzed in the LumiSizer Dispersion Analyser by co-supervisor Zeeshan Ali. LumiSizer is a sedimentation-based particle size and dispersion stability analyzer [88]. According to the LumiSizer measurements, the samples where 50 mL and 100 mL solvent were applied, showed similar velocity profiles. However, the sample synthesized with 150 mL solvent settled noticeably quicker, implying that it may contain bigger aggregates, which is undesirable.

Based on the findings of LumiSizer and the limited time available for this research, it was decided to continue with 50 mL and 100 mL solvent volumes. However, it should be noted that the LumiSizer data alone is not a solid finding on which to base this decision, and it is recommended to conduct additional research on larger solvent volumes in the future. Since a solvent volume of 20 mL was utilized in the work of Ali [89], it was chosen to also include a volume of 20 mL solvent in addition to 50 mL and 100 mL for the experimental design. In that way, the findings of this study could be directly compared to the work of Ali [1]. Furthermore, working with a smaller volume of solvent is preferred because it minimizes consumption, which is particularly essential in the case of up-scaling when the solvent quantity is substantially increased.

4.3 Characterization of Amine-Functionalized Silica Coated Iron Oxide Nanoparticles

An experimental design of amine-functionalized silica coating of IONPs was carried out based on the findings in the specialization project and the preliminary experiments provided in Section 4.2. In the following sections, a detailed analysis and discussion of the resulting amine-functionalized silica coated IONPs are presented. The experiments were carried out according to the protocol provided in Section 3.3. STEM images obtained from all experiments can be found in Appendix B.

4.3.1 Design of Experiments

In this study, three distinct silanization input reaction parameters were varied: the type of IONPs coated, the volume of solvent, and the weight proportion of 3-aminopropyl triethoxysilane (APTES) to the total weight of added APTES and tetraethyl orthosilicate (TEOS). It should be noted that the weight proportion of APTES to the total weight of APTES and TEOS is often referred to as 'wt% of APTES' in this discussion. Furthermore, the theoretically determined amount of obtained silica from TEOS and APTES was kept constant at 49 mg silica in all experiments. The detailed calculations regarding this can be found in Appendix A, Section A.0.1.

During the specialization project, it was discovered that in the event where TD-IONPs were coated with silica, the particles were to a greater extent spherical and marginally smaller, compared to

silica coated CP-IONPs. Due to differences in morphologies, it was decided to conduct experiments involving both TD-IONPs and CP-IONPs for the experimental design in this research as well. The characterization of the TD-IONPs and CP-IONPs that are utilized for coating is presented in Section 4.1. Furthermore, it was determined to vary the total volume of solvent to 20 mL, 50 mL and 100 mL, in accordance with the findings from the preliminary results reported in Section 4.2. In the specialization project, all the experiments were conducted with 25 wt% of APTES. It is desired to obtain a combination of amine- and hydroxyl groups on the surface of the silica coated IONPs. In this study, it was decided to investigate the effects when the quantity of APTES in the synthesis is reduced, hence experiments with 25 wt%, 15 wt%, and 5 wt% APTES were conducted. Overall, a complete full factorial design with two center points was generated using the software JMP. Additionally, control experiments were preformed with both 0 wt% APTES and 100 wt% APTES. Table 3.2 presents the full set of experiments with reaction conditions.

Each experiment is labeled with a sample name comprised of three terms in accordance with the varying input parameters. The first term, denoted by 'S100', 'S50', and 'S20', signifies 'solvent amount' and total volume (mL) of solvent, which includes the combined ethanol and MQ-water added. The middle term indicates the wt% of APTES. The last term represents the IONPs type, denoted by 'TD' and 'CP' for experiments where IONPs synthesized by thermal decomposition and co-precipitation are coated, respectively. For example, S50-15%-TD represents an experiment in which thermal decomposition IONPs were coated under conditions of 50 mL solvent and 15 wt% of APTES.

4.3.2 Control Experiments

To get a better understanding of the function of APTES in the silanization reaction, control experiments were conducted with only APTES (S100-100%-TD, S100-100%-CP) and only TEOS (S100-0%-TD, S100-0%-CP) used as silica precursors.

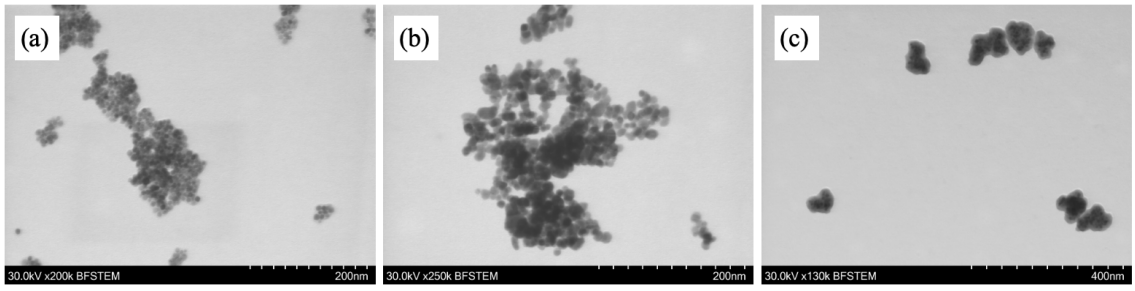

Figure 4.7: Bright-field TEM images of sample (a) S100-100%-TD, (b) S100-100%-CP and (c) S100-0%-TD

Only APTES as the Silica Precursor

In Figure 4.7, image (a) and (b) shows the representative bright-field TEM images for samples S100-100%-TD and S100-100%-CP, respectively, in which pure APTES is used as a silica precursor. The mean hydrodynamic size with standard deviation of sample S100-100%-TD was obtained to be 312±22 nm, while for sample S100-100%-CP it was exceeding the upper measuring limit of DLS (>10 000 nm). The mean zeta potentials with standard deviations were 17±0.2 mV and -2.4±0.0 mV for experiment S100-100%-TD and S100-100%-CP, respectively. Additionally, the ninhydrin assay revealed no absorbance signal of amine groups on the particles.

The bright-field TEM images, in the event where only APTES is applied, display simply the IONPs, with no visible silica covering the IONPs. The results from the ninhydrin assay support this observation, as it identified no amine groups, which would have been present if the IONPs had been coated with pure APTES. Those observations are consistent with the findings of Digigow *et al.* [53], which also observed tiny aggregates and virtually no silica coating of the IONPs. As previously mentioned in Section 2.4.1, according to Van Blaaderen *et al.* [80], hydrolyzed APTES molecules may create six- or five-membered chelate rings in basic pH systems. Due to steric effects, such ring formation may inhibit the condensation of APTES itself and lead to no precipitated particles. Furthermore, Chen *et al.* [81] demonstrated the formation of a strong hydrogen bond between the amine group and silanol group on two neighboring APTES molecules, which may hinder further condensation with other APTES molecules if the interaction is sufficiently strong. Consequently, these phenomena might account for the no visible coating of the IONPs observed in Figure 4.7 (a) and (b). Although it appears that the particles are not coated with silica, zeta potentials indicate that they are more unstable than the bare TD-IONPs and CP-IONPs discussed in Section 4.1. The zeta potential of sample S100-100%-CP is near the isoelectric point, indicating that the particles may have aggregated due to a lack of electrostatic stabilization, which might explain the huge hydrodynamic size.

Only TEOS as the Silica Precursor

Image (c) in Figure 4.7 shows the representative bright-field TEM images for samples S100-0%-TD, in which pure TEOS is used as a precursor, and the bright-field TEM images from experiment S100-0%-CP showed similar particles. The mean hydrodynamic sizes and zeta potentials with standard deviations were 157±2 nm and -36.3±0.2 mV for experiment S100-0%-TD and 167±1 nm and -42.8±0.2 mV for experiment S100-0%-CP. In addition, no signals of amine groups on the surface of the particles were identified by the ninhydrin assay.

The bright-field TEM images displayed that IONPs have been coated with a thin layer of silica in experiments S100-0%-TD and S100-0%-CP. The negative zeta potential values are consistent with expectations, given that TEOS contributes to surface hydroxyl groups, which are negatively

charged for pH close to 7. In addition, the results of the ninhydrin assay are as anticipated, since TEOS chemically does not possess amine groups. Moreover, it is noteworthy that Digigow *et al.* [53] reported a significant increase in the incorporation of IONPs in the silica matrix when TEOS alone was applied, compared to the combination of TEOS and ATPES. They have proposed that this finding may be due to the presence of APTES which prevents initial IONPs aggregation. This observation seems to be evident from the bright-field TEM images in this research, however, the size of the IONPs core and silica thickness was not investigated further in these experiments due to time limitations.

On the basis of these findings and the research conducted by Chen *et al.* [81], it is reasonable to assume that morphologies of the silica coated IONPs are primarily controlled by the hydrolysis and condensation of TEOS. APTES alone does not produce visible silica coating on IONPs, which may be due to hydrolyzed APTES reacting with itself and inhibiting condensation to particles.

4.3.3 Elemental Mapping

This section and the following sections discuss the silica coated IONPs obtained from the full factorial experimental design. The chemical composition of the particles was mapped using EDS in conjunction with STEM. There are typically three possible outcomes of the synthesis: IONPs, silica particles, and silica coated IONPs. Consequently, EDS was utilized to determine the composition of the obtained particles.

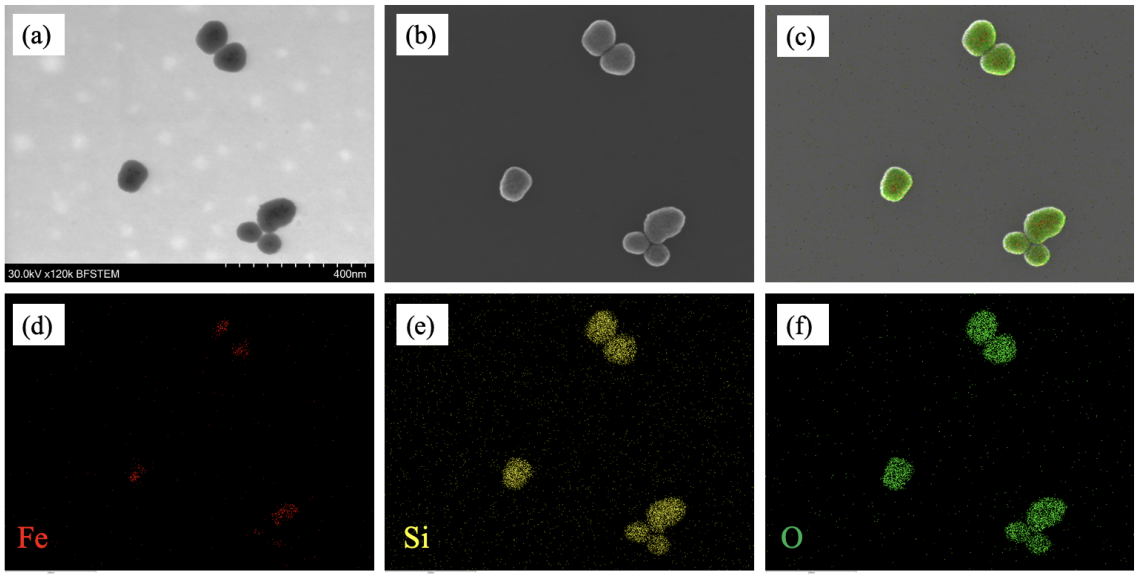

Figure 4.8: Different images of the same particles from experiment S50-5%-TD. (a) Bright-field TEM image, (b) SEM electron image, (c) EDS mapped image of both silicon, oxygen and iron, (d) mapped iron, (e) mapped silicon and (f) mapped oxygen.

Figure 4.8 presents different images of five particles that were obtained from experiment S50-5%-TD. Image (a) is a bright-field TEM image with a scale bar, revealing that all of the particles contained darker TD-IONP cores. Furthermore, image (b) shows an electron image of the particles that were mapped using EDS, and it can be seen that the particles produce signals of iron (Fe), silicon (Si) and oxygen (O) from image (c)-(f). Upon close study of image (d), it can be seen that the small dark regions within the particles in the bright-field TEM image correspond visually to the iron signals. In addition, as seen in images (e) and (f), the entire particle surface exhibits silicon and oxygen signals. This indicates that all five particles were silica coated TD-IONPs.

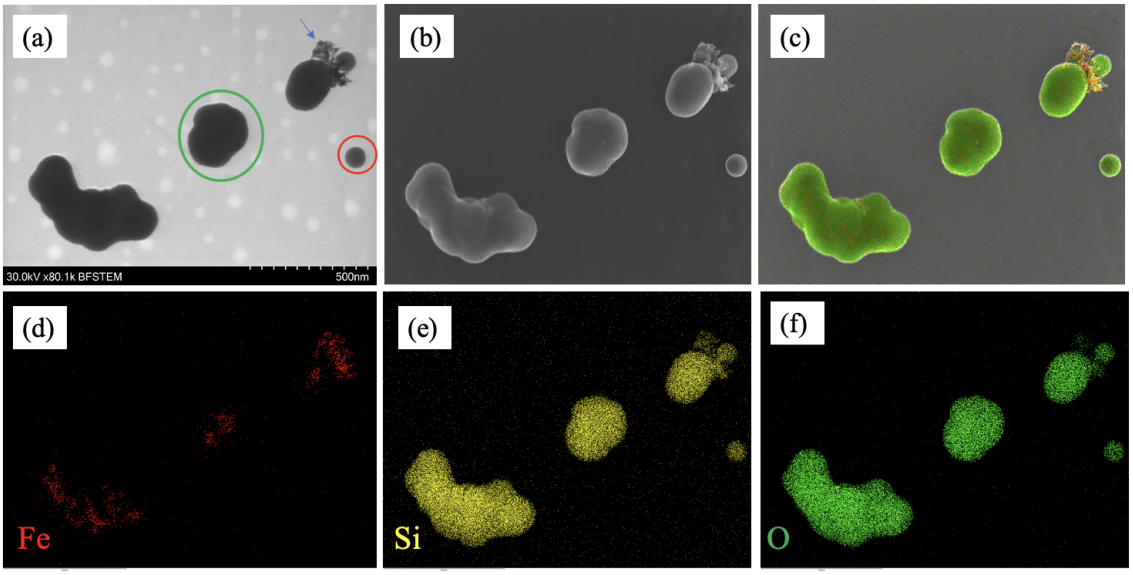

Figure 4.9: Different images of the same particles from experiment S20-15%-CP. (a) Bright-field TEM image, (b) SEM electron image, (c) EDS mapped image of both silicon, oxygen and iron, (d) mapped iron, (e) mapped silicon and (f) mapped oxygen.

On the other hand, Figure 4.9 presents different images of particles that were obtained from experiment S20-15%-CP. Similar as Figure 4.8, image (a) is a bright-field TEM image, while image (b) shows an electron image that were mapped by EDS, and the particles produced signals of iron (Fe), silicon (Si) and oxygen (O) as seen from image (c)-(f). Visually, based on the bright-field TEM image, IONPs inside the larger particles, such as the one highlighted by the green circle, could not be recognized clearly. The existence of IONPs inside those particles, however, is shown by the iron signals seen in image (d). In addition, smaller spherical particles and clusters that appear to be IONPs are visible in image (a), as indicated by the red circle and blue arrow, respectively. The elemental signals from images (c)-(f) reveal that these are, respectively, bare silica particles and free IONPs that may contain a thin layer of silica. Consequently, this indicates that this sample contains three different particle morphologies, being silica coated IONPs, bare silica particles and clusters of IONPs that may contain a thin, invisible layer of silica.

4.3.4 Morphologies

In general, the bright-field TEM images revealed that each of the experiments consisted of one of the three particle composition types depicted in Figure 4.10. TEM images of all experiments can be found in Appendix B. Image (a) shows single spaced silica coated IONPs of similar dimensions, assigned as Type I. Image (b), assigned as Type II, depicts two distinct particle morphologies, including silica coated IONPs and clusters of IONPs with a thin layer of silica coating, which is pointed out by the blue arrow. Image (c), assigned as Type III, reveals large silica coated IONPs, smaller bare silica particles, and clusters of IONPs with a thin silica coating, as marked by the green circle, red circle, and blue arrow, respectively. The Type III particle composition class corresponds to the particles identified by EDS in Figure 4.9, which confirms that samples of this type consist of the three distinct particle morphologies described.

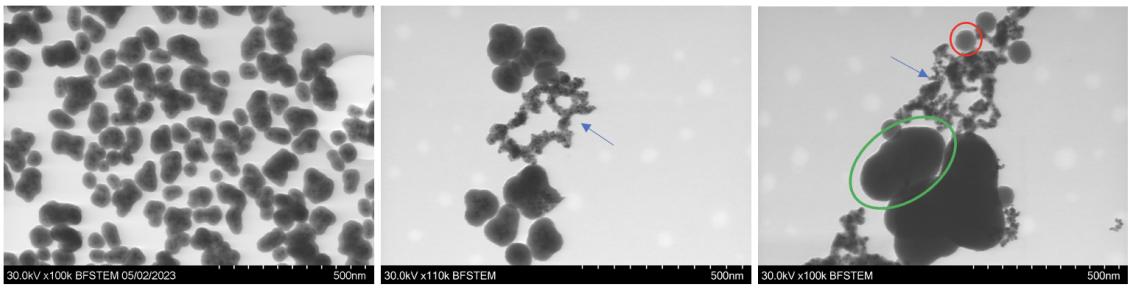

(a) Type I (b) Type II (c) Type III

Figure 4.10: Bright-field TEM images of sample (a) S100-5%-CP, (b) S60-15%-TD and (c) S50-25%-CP. The scale is identical of all the images.

Table 4.1: An overview of the particle composition types in all the experiments.

	TD			**CP**		
	5%	**15%**	**25%**	**5%**	**15%**	**25%**
S20	Type I	Type III	Type III	Type II	Type III	Type III
S50	Type I	Type II	Type II	Type I	Type II	Type III
S60	-	Type II	-	-	Type II	-
S100	Type I	Type I	Type I	Type I	Type I	Type II

Table 4.1 provides an overview of the different composition types from Figure 4.10 that were observed from each experiment. The bold headers of the table correspond to the labeled experiment names as explained in section 4.3.1. Although all samples are classified into one of these composition categories, it should be noted that minor exceptions were discovered. For instance, in some experiments classified as Type I, the presence of uncoated IONPs was observed, but their proportions were considered negligible compared to other observations. Furthermore, it is noteworthy that the particles did not exhibit perfect spherical shapes, and fused particles were observed along-

side single spaced particles in several samples. For silica-coated IONPs, it is observed that the silica layer forms nearly uniformly around the aggregated cores of IONPs, as a multiple IONPs core - silica shell structure. Consequently, this made it difficult to distinguish whether the particles were overlapping, fused together, or consisted of an anisotropic shaped IONPs core.

From Table 4.1, it appears that the composition type and particle morphologies vary consistently as the solvent volume and wt% of APTES are varied. When lower solvent volumes, such as 20 mL and 50 mL, were used, Type II and Type III compositions dominated, and individual spherical silica coated IONPs were observed only when 5 wt% of APTES was utilized. In addition, it appears that the number of different particle morphologies (from Type I to III) was increased as the wt% of APTES was increased. In contrast, when 100 mL of solvent was utilized, there were almost only individual silica coated IONPs observed. All of the above findings apply to both silica coated TD-IONPs and CP-IONPs experiments.

The findings in the study of Digiow *et al.* [53] and in the specialization project, did not demonstrate the different morphologies as those observed in experiments assigned as composition Type III. However, in both of those studies, a solvent volume of 100 mL was utilized, which primarily led to the formation of individual silica-coated IONPs, which is also consistent with the outcomes of the experiments in this study in which 100 mL of solvent was used.

The transition in morphologies from spherical silica coated IONPs to both larger silica coated IONPs, small bare silica particles, and clusters of IONPs, is observed when the solvent quantity is lowered and the wt% of APTES is raised. This shift is significantly connected to the concentration of APTES in the reaction, such as for higher concentrations of APTES (3.9 mM - 9.8 mM), distinct morphologies, denoted as Type III are seen, while for lower concentrations (0.4 mM - 2.4 mM) only morphologies of Type I and II are observed. As stated in Section 2.4.1, previous research by Chen *et al.* [81] demonstrated that APTES itself acts as a catalyst in the Stöber reaction in addition to ammonia solution. The observed shift in morphologies may therefore be due to the increased catalytic activity of APTES, which influences the rate of hydrolysis and condensation, and consequently the resulting particle morphologies. However, the exact underlying mechanism behind the observed differences in morphologies is unknown.

Figure 4.11 shows bright-field TEM images from experiment (a) S50-5%-TD and (b) S50-5%-CP where only the type of coated IONPs were different. On the basis of these two images, it is challenging to observe differences in particle morphologies, and in general, no significant differences in particle morphologies were observed as the type of coated IONPs was altered, taking into account the same composition types.

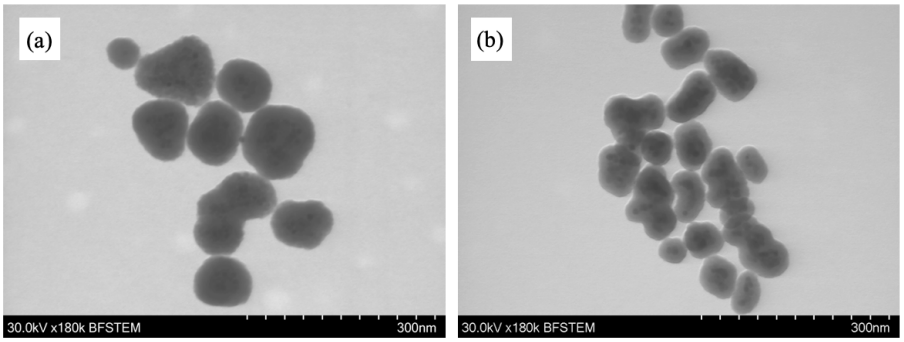

Figure 4.11: Bright-field TEM images of sample (a) S50-5%-TD and (b) S50-5%-CP which shows that the morphologies are similar for coated TD-IONPs and CP-IONPs.

4.3.5 Hydrodynamic Particle Sizes

The hydrodynamic sizes of the nanoparticles were determined using DLS. It was previously determined by our research group, that a light transmittance range of 40% to 60% provides an optimal signal-to-noise ratio for measurements of these types of nanoparticles. Consequently, the samples for DLS measurements were diluted to fall within this transmittance range, typically at a concentration of 0.5 mg/mL of silica coated IONPs in MQ-water. For the experiments consisting of the three distinct particle morphologies, denoted as Type III in Section 4.3.4, a rapid measurement approach was employed. This involved performing five runs of five seconds per measurement, resulting in a total of six measurements per sample. On the other hand, the remaining samples were measured in an automatic mode, with a maximum of 60 runs of 10 seconds per measurement, resulting in a total of three measurements per sample.

Figure 4.12 shows graphs of typical intensity weighted DLS measurements of samples of the experiments. Graph (a) depicts the six measurements of sample S20-15%-TD, and it clearly demonstrates that the sample contained distinct particle populations. However, it is difficult to identify their precise intensity maximums, as they shift from measurement to measurement. Additionally, the graphs display huge hydrodynamic particle sizes that are well beyond the desired size. From the bright-field TEM images it was observed silica coated IONPs up to 1000 nm in size, as well as massive clusters of IONPs. Consequently, it may be reasonable that the intensity tops are of the DLS measurements are larger that 1000 nm. These multiple intensity peaks of large sizes, shown in graph (a), were typically observed for all the experiments where the bright-field TEM images revealed three separate particle morphologies.

Following this, graphs (c) and (d) in Figure 4.12 demonstrate common particle measurements for samples of composition Type II and Type I, respectively. Graph (d) depicts sample S100-50%-CP and shows a sharp single peak at 230 nm, whereas graph (c) depicts sample S50-15%-TD, which shows a peak at 250 nm with higher polydispersity towards larger sizes. The bright-field

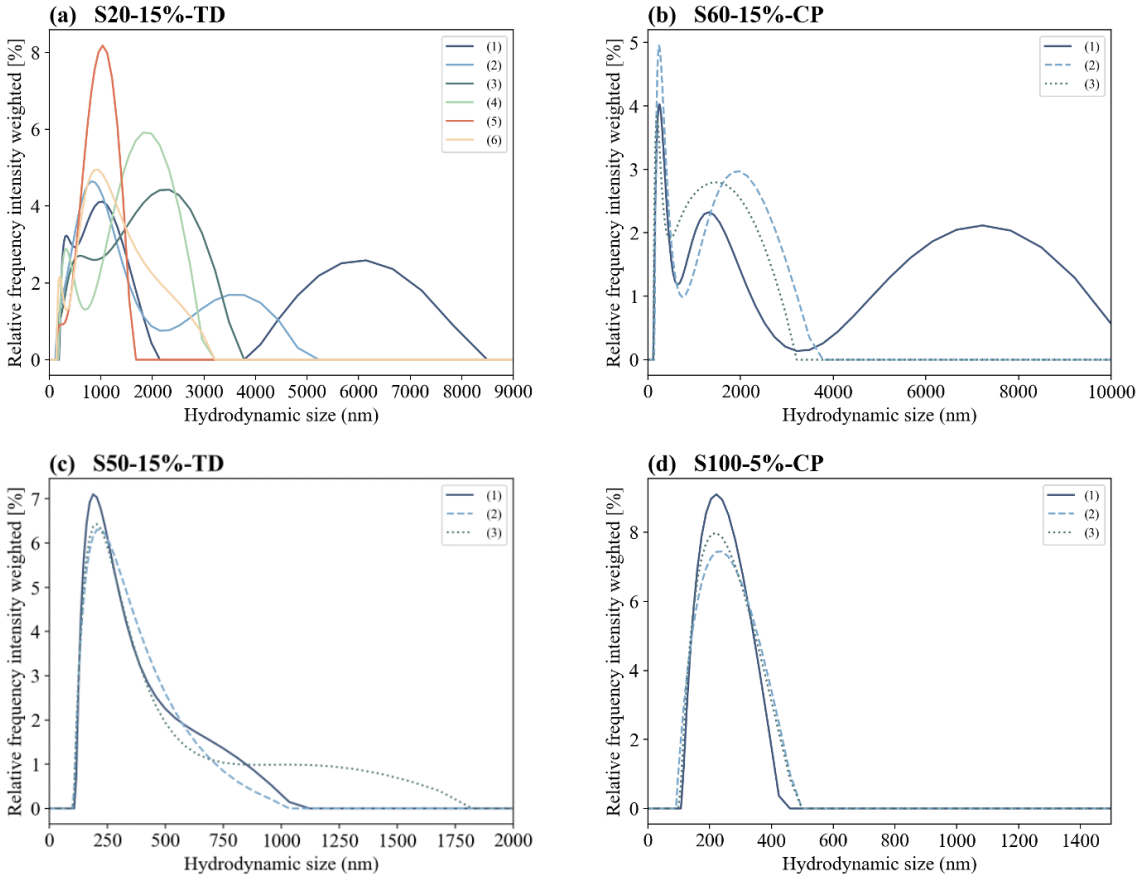

Figure 4.12: DLS measurements of sample (a) S20-15%-TD, (b) S60-15%-CP, (c) S50-15%-TD and (d) S100-5%-CP.

TEM images revealed that samples of Type II, such as S50-15%-TD, contained some aggregates of IONPs coated with a thin layer of silica in addition to silica coated IONPs. Thus, this broader curve of larger sizes may be attributed to aggregated morphologies. Furthermore, sample S60-15%-CP, shown in graph (b), distinguished from the rest of the measurements of samples of Type II, and showed clearly a distinct particle top around 2000 nm in addition to a top at 250 nm. According to this result, sample S60-15%-CP may have contained larger aggregates.

Figure 4.13 shows bar plots of the mean hydrodynamic sizes with standard deviations obtained from (a) silica coated TD-IONPs and (b) silica coated CP-IONPs. The samples are grouped together on the x-axis according to the wt% of APTES used, while they are positioned in ascending order according to the volume of solvent within each group. The experiments that contained three different types of particle morphologies, denoted as Type III in Section 4.3.4, are excluded from these bar graphs because their particle morphologies were distinct, and the intensity maxima shifted across measurements. In addition, the S60-15%-CP sample is also excluded because distinct particle populations were evident as seen from graph (b) in Figure 4.12.

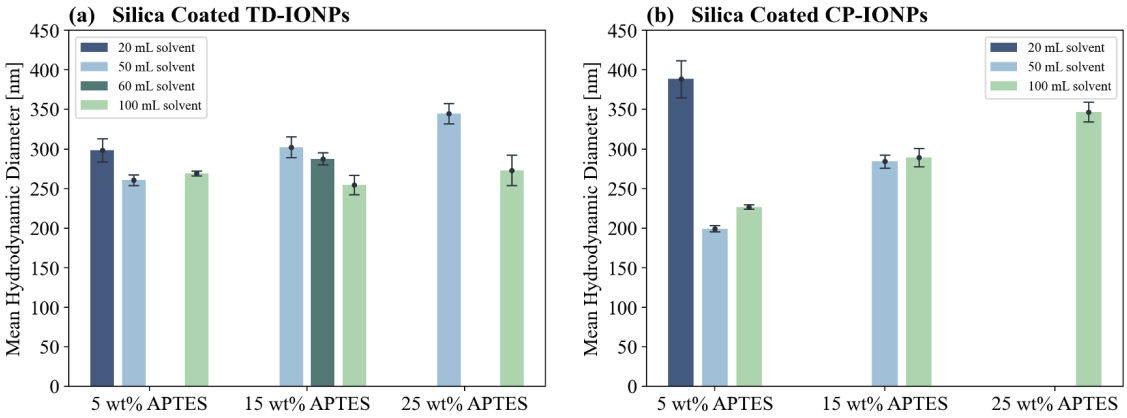

Figure 4.13: Mean hydrodynamic diameters with standard deviations for silica coated (a) TD-IONPs and (b) CP-IONPs.

In general, the mean hydrodynamic diameter of silica-coated TD-IONPs ranged from approximately 288 nm to 345 nm, while for silica-coated CP-IONPs, it varied between approximately 199 nm and 388 nm. These findings are higher than those reported in the study conducted by Digiow *et al.* [53], where the hydrodynamic sizes ranged from about 70 nm to 180 nm. In addition, the results of Digiow *et al.* revealed a significant increase in the hydrodynamic size as the wt% of was APTES increased. From Figure 4.13, when the wt% of APTES is varied while the other input parameters are kept constant, a slight increase in hydrodynamic size is observed, except in the case of coated TD-IONPs with 100 mL solvent. However, no significant trends in hydrodynamic size differences, as input parameters were varied, were identified in this research. In some of the experiments, denoted as Type II in Section 4.3.4, there were found larger aggregates of IONPs with thinner layers of silica in addition to the silica coated IONPs. The quantity and extent of these aggregated structures, which appear to be random from sample to sample, may be the reason for the lack of a distinct trend, making it difficult to draw conclusions about how input parameters may have affected hydrodynamic size.

4.3.6 Dry Particle Sizes and Silica Shell Thicknesses

Dry particle sizes were determined by using the software ImageJ, where 100 random particles were counted manually from STEM images for each experiment. Since the majority of the particles were not perfectly spherical, the mean of the short axis and the long axis of a particle were measured, as illustrated by the crossed arrows in Figure 4.14. The thicknesses of the silica coating were determined the same way by using the ImageJ, with 200 random silica shells counted manually from STEM images for each sample. Figure 4.14 illustrates how the thickness is determined by measuring the distance between the outer dark IONPs core and the outer border of the silica coated IONPs. The thickness of the silica coating may differ at various positions on a particle, and therefore, two to three measurements were performed on each particle. Only individual silica coated

IONPs from samples of class Type I and Type II from Section 4.3.3, were taken into account for determining the dry sizes and the silica shell thicknesses.

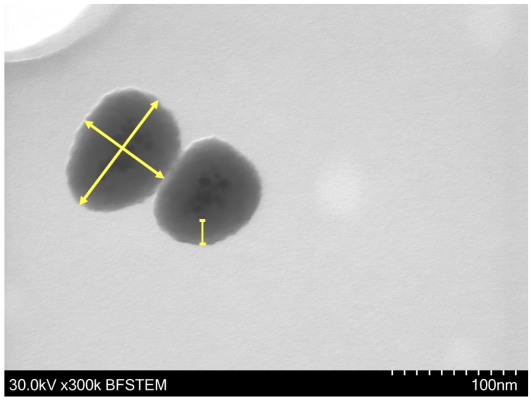

Figure 4.14: The short and the long axis of a particle is demonstrated by the crossed yellow arrows. The silica thickness distance is illustrated by the short yellow line.

Figure 4.15 and 4.16 shows bar plots of the measured mean (a) dry diameters and (b) silica shell thicknesses with standard deviations of silica coated IONPs, where TD-IONPs and CP-IONPs were applied, respectively. The samples are grouped together on the x-axis according to the wt% of APTES used, while they are positioned in ascending order according to the volume of solvent within each group. For silica coated TD-IONPs, the diameter ranged from approximately 80 nm to 105 nm, and the silica coating thickness ranged from 24 nm to 35 nm. While the diameter of silica-coated CP-IONPs varied from approximately 61 nm to 99 nm and the coating thickness varied from 14 nm to 28 nm. All over, by observing Figure 4.15 and 4.16, it is apparent that the trend of the measured dried diameters matches the trend of the measured silica shell thicknesses. By subtracting the measured silica shell thickness from the mean dry diameter, the diameters of the IONPs core are calculated to be between 23 nm and 48 nm for TD-IONPs and between 33 nm and 45 nm for CP-IONPs.

As seen in Figure 4.15 and 4.16, most of the particle sizes and silica thicknesses increase slightly when the wt% of APTES is increased and other parameters are kept constant, which was also observed for the hydrodynamic sizes. This applies generally, except for the size in the event of coated TD-IONPs and 50 mL solvent, and the silica shell thicknesses in the event of coated TD-IONPs for 50 mL and 100 mL solvent. Moreover, it seems that the type of IONPs had the greatest effect on particle size and silica thickness. In all experiments, except for the one in which 60 mL solvent and 15 wt% APTES were used, coated TD-IONPs generated larger particle diameters and shell thicknesses than coated CP-IONPs, when all other reaction conditions were held constant. In comparison to the specialization project, the dry particle sizes obtained in this study were slightly smaller for all experiments where TD-IONPs were used compared to CP-IONPs. However, it should be noted, however, that the reaction conditions were different in the specialization project,

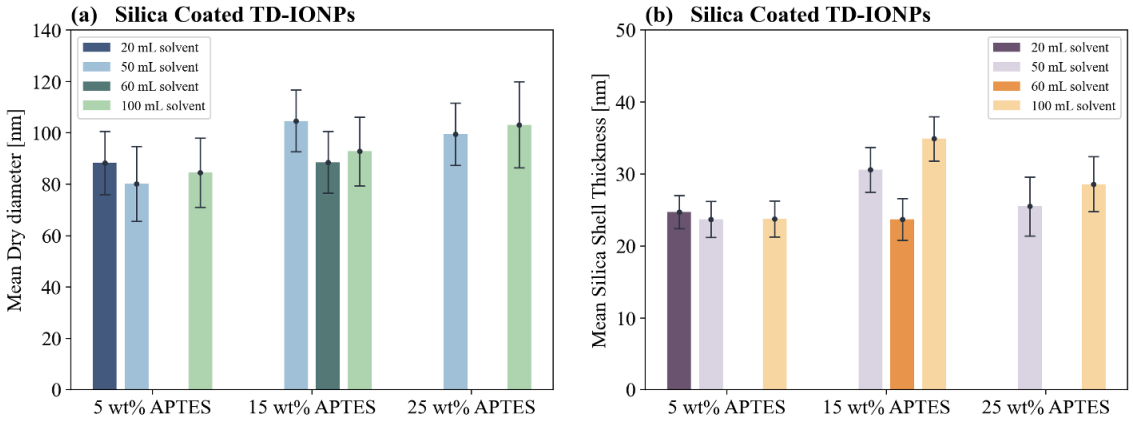

Figure 4.15: (a) Mean dry diameter and (b) mean silica shell thickness with standard deviations from experiments where TD-IONPs were utilized.

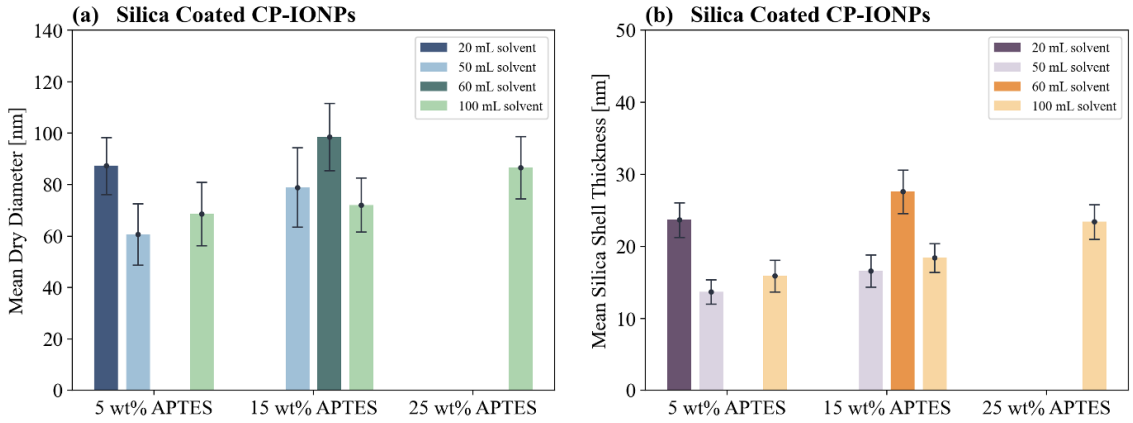

Figure 4.16: (a) Mean dry diameter and (b) mean silica shell thickness with standard deviations from experiments where CP-IONPs were utilized.

resulting in dry particle sizes ranging from approximately 90 nm to 300 nm.

It is important to highlight that the dry size measurements were conducted on a limited number of 50-100 particles due to time constraints. As a result, the standard deviations are relatively high, and there may be uncertainties associated with the measurements. Considering the observed standard deviations and the minor variations in size and silica shell thickness when varying the input parameters, the influence of these parameters does not appear to be particularly significant in this study.

4.3.7 Magnetic Properties

In Figure 4.3, it was demonstrated that the synthesized TD-IONPs and CP-IONPs were super-paramagnetic, which is an important and unique characteristic. As a consequence, it is crucial

that the magnetic property of the particles remains subsequent to silica coating. VSM was used to measure the magnetization curves of the silica coated IONPs, and the data were normalized by the mass of the sample. Given that the magnetization curves were normalized by mass, it is preferable to have sufficiently large sample masses, as the overall error could be quite substantial for small sample masses as compared to larger sample masses. Consequently, the masses of all VSM samples ranged between 7-10 mg silica coated IONPs.

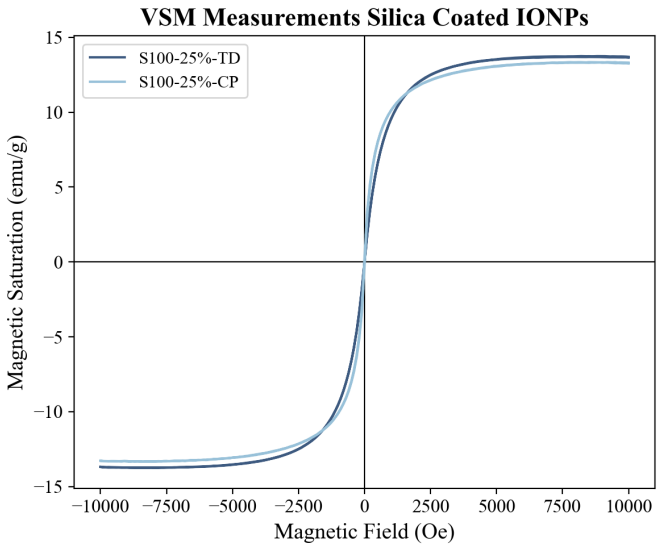

Figure 4.17: Magnetization curves for experiments S100-25%-TD and S100-25%-CP.

Figure 4.17 presents the magnetic measurements of silica coated IONPs from experiments S100-25%-TD and S100-25%-CP. The absence of a hysteresis loop and zero coercivity indicate the superparamagnetic behavior of the silica-coated IONPs. This behavior was consistently observed in all experiments. Table 4.2 provides an overview of the magnetization saturation values from the magnetic measurements for all the experiments. The bold headers of the table correspond to the labeled experiment names as explained in Section 4.3.1.

Table 4.2: Magnetization saturation values for all experiments.

	TD			**CP**		
	5%	**15%**	**25%**	**5%**	**15%**	**25%**
S20	12.7 emu/g	12.1 emu/g	12.7 emu/g	13.9 emu/g	12.0 emu/g	11.5 emu/g
S50	14.5 emu/g	13.1 emu/g	12.9 emu/g	13.4 emu/g	13.1 emu/g	13.0 emu/g
S60	-	11.4 emu/g	-	-	11.0 emu/g	-
S100	15.5 emu/g	13.3 emu/g	13.7 emu/g	13.4 emu/g	11.7 emu/g	13.3 emu/g

Table 4.2 shows that measured saturation magnetization values are relatively similar and span the range of 11.0 emu/g to 15.5 emu/g. As previously stated, the magnetic saturation values for silica

coated IONPs are lower than those for bare IONPs, since the non-magnetic silica shell lower the magnetic saturation when the value is normalized by the total particle mass. From Section 4.1, bare TD-IONPs and CP-IONPs had similar magnetization saturation values of 52.1 emu/g and 57.0 emu/g, respectively. Consequently, since the ratio of IONPs to the amount of silica precursor was kept fixed in all of these experiments, it was expected that the variations in magnetic saturation would be small unless there was any loss of IONPs or silica during the synthesis.

4.3.8 Zeta Potentials

As discussed in Section 2.4, the presence of organosilanes such as APTES can affect the surface charge and provide improved stability of silica coated IONPs. Figure 4.18 shows plots of the measured mean zeta potentials with calculated standard deviations out of three measurements, for (a) silica coated TD-IONPs and (b) silica coated CP-IONPs, as a function of solvent volume. All the readings revealed positive charges, ranging from 22.6±0.3 mV for sample S50-5%-CP to 40.6±0.3 mV for sample S100-15%-TD.

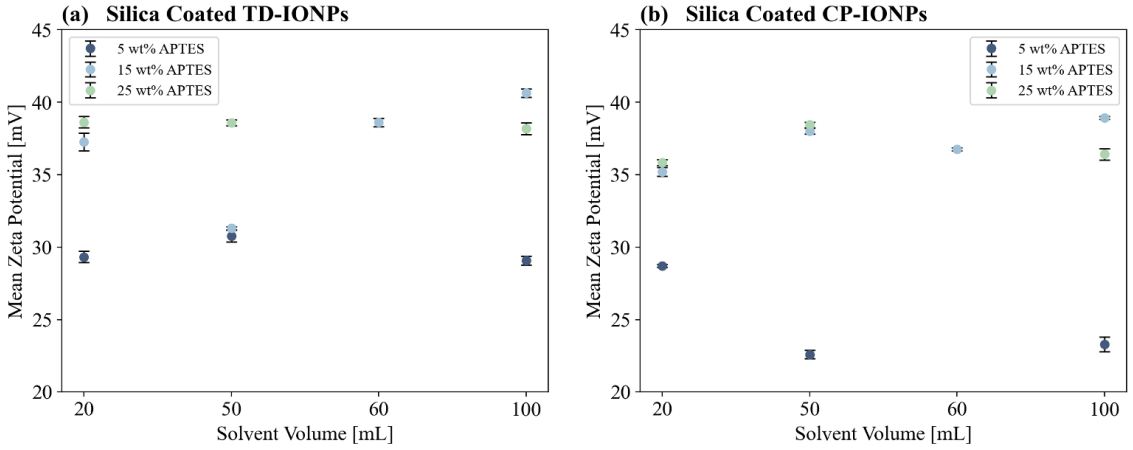

Figure 4.18: Mean zeta potentials with standard deviations for silica coated (a) TD-IONPs and (b) CP-IONPs as a function of solvent volume.

As shown in Figure 4.18, a significantly increased shift in the zeta potential is observed when the amount of APTES is increased from 5 wt% to 15 wt% while all other reaction conditions remained unchanged. On the other side, the increase from 15 wt% to 25 wt% of APTES gave similar zeta potential values, and in some experiments, the values for the 15 wt% of APTES samples were even slightly higher than the for the 25 wt% of APTES samples. The only outpointed exception to this trend is the measured zeta potential from experiment S50-15%-TD, in which additional measurements were conducted that confirmed the plotted value.

As previously stated in Section 2.4.1, silica surfaces of TEOS are negatively charged above its isoelectric point (pH >2), due to the presence of deprotonated silanol groups (SiO^-). However, APTES provides protonated amine groups (NH_4^+) in water, and consequently, it was expected that

the presence of APTES would influence the measured zeta potentials and stability of the particles. As a reference, from Section 4.3.2, the zeta potentials of particles coated with only TEOS were measured to be -36.3±0.2 mV and -42.8±0.2 mV for experiments S100-0%-TD and S100-0%-CP, respectively. The increase in zeta potential upon the addition of APTES, indicates the presence of amine groups on the surface of the particles. Moreover, the increase in stability from 5 wt% to 15 wt% of APTES suggests that the fraction of surface amine groups increased during this change in APTES concentration. However, additional characterization is required to confirm the presence and potential quantity of APTES.

In comparison with the study by Digigow *et al.* [53], they observed a net positive surface charge only after 10 wt% of applied APTES, while at higher APTES concentrations such as 25-30 wt%, the increase in zeta potentials was less prominent. However, it should be noted that the particles in this research were not constructed of the same input quantities as of the research of Digigow *et al.*. While net positive surface charges were seen in all of the experiments provided in Figure 4.18, there was also a non-significant change at higher concentrations, of 15-25 wt% in this instance, in agreement with Digiow *et al.*. As hypothesized by Digiow *et al.*, this observation may be due to a saturation of amine groups on the surface of the silica coated IONPs.

It is important to highlight that the pH of the sample solutions, which affects the zeta potentials, was not explicitly measured for the samples. The samples were diluted with MQ-water prior to measurement to achieve a light transmittance of 40% - 50%, as reported in Section 3.6.1. Consequently, for future studies, it is recommended that the measurements are done at a fixed pH for a more accurate comparison.

4.3.9 Quantification of Surface Amine Groups

The colorimetric ninhydrin assay, which is described in Section 3.4, was used to confirm the existence and analyze the quantity of amine groups (-NH_2) found on the surface of the silica coated IONPs. Figure 4.19 shows bar plots of the content of free amine groups per grams of (a) silica coated TD-IONPs and (b) silica coated CP-IONPs, as a function of the solvent volume. It displays the average of two measurements with calculated standard deviations. The measurements confirmed that all the samples contained amine groups, ranging from 72±8 μmol/g for sample S20-5%-TD to 3322±74 μ mol/g for sample S100-25%-CP. No significant trend in variations was observed when the solvent volume and type of IONPs were varied. However, a notable trend in variations was observed for different wt% of APTES, which is explained below.

As shown in Figure 4.19, the number of accessible amine groups on the surface of the silica coated IONPs increases with increasing wt% of APTES. This is consistent with expectations and strengthens the previous results reported in Section 4.3.8, where enhanced stability from 5 wt% to 15 wt% of APTES was seen. From the zeta potential measurements, it was also hypothesized

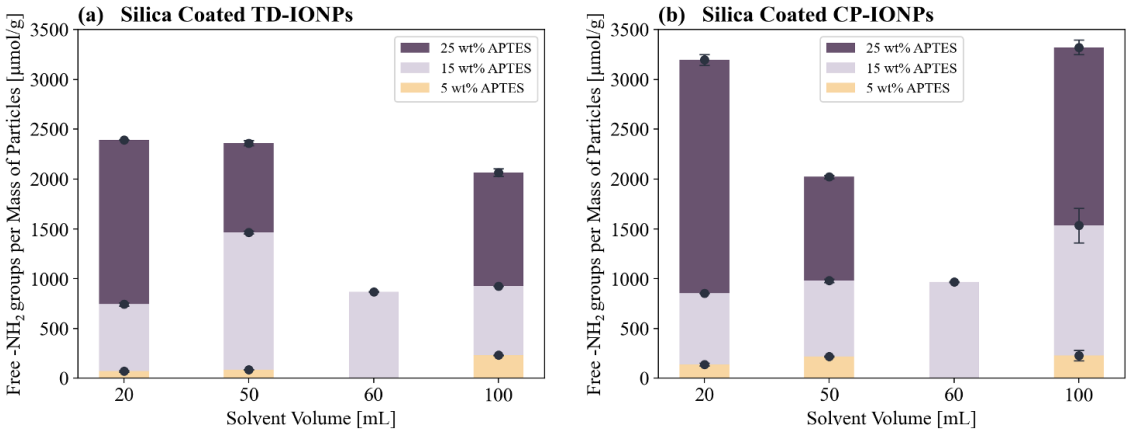

Figure 4.19: Content of free amine groups (NH_2) per grams of silica coated (a) TD-IONPs and (b) CP-IONPs as a function of solvent volumes.

that the surface may be saturated with amine groups after 15 wt% of APTES. However, this is not indicated by the data from Figure 4.19, where the amine content is raised further from 15 wt% to 25 wt% of APTES. Generally, the measured amine content values were in the range of 72-232 μmol/g, 743-1535 μmol/g and 2021-3322 μmol/g, for 5, 15 and 25 wt% of APTES, respectively.

The colometric ninhydrin test utilized in this study was inspired by the method proposed by Karade *et al.* [87], which investigated spherical IONPs functionalized by a layer of APTES. Karade *et al.* determined an amine content of 41.5 μmol/g, corresponding to a fractional monolayer coverage of 96.6% of APTES. The assumption made in their study was that perfectly spherical silica particles would have a monolayer coverage of APTES equivalent to the presence of four 3-aminopropylsilane molecules per square nanometer of the surface [87]. This assumption is supported by several relevant studies. For instance, Kunc *et al.* [84] and Sun *et al.* [86] conducted research using alternative ninhydrin assays on amine-functionalized silica nanoparticles within the size range of 20 nm to 120 nm. These studies revealed that the amine content of the nanoparticles was lower than anticipated for monolayer coverage.

For instance, assuming that the particles from experiments S100-5%-TD and S100-25%-TD were spherical silica particles with the respective dry diameters provided in Section 4.3.6, the above assumption would result in approximately 1.3 and 14 times the expected monolayer coverage, respectively. Detailed information regarding the calculations of APTES coverage can be found in Appendix C. As a result, the values obtained in this study are significantly higher than similar studies based on the assumption of four 3-aminopropylsilane molecules per square nanometer of the surface for monolayer coverage. This raises concerns about the reliability of the ninhydrin assay, since it is designed to measure only the accessible amines in solution.

On the contrary, the calculations to obtain fractional monolayer coverage are based on an approximation that assumes ideal spherical particles of uniform size. It should be noted that the particles

obtained in this study were not perfectly spherical, and their sizes and surface roughness displayed variations. These variations have an impact on the actual specific surface area (SSA), which is a critical factor in the calculation. Furthermore, it is important to note that the silanization procedure utilized in this study is a one-pot synthesis, which makes it impossible to control the distribution of APTES throughout the silica matrix. The ninhydrin reagent was used in excess for the analysis, and it is unknown whether the ninhydrin may have interacted with amine groups present within the silica matrix, which could have become accessible as the primary accessible groups underwent the reaction. These factors may have contributed to the observed higher calculations and measurements of amine content.

The calibration curve was constructed by using known concentrations of octylamine as the amine-containing species. Octylamine was chosen over amine standards such as leucine and APTES based on the findings of Sun *et al.* [86]. Measurements of constructed calibration curves can be found in Appendix D. It was observed that at lower concentrations, the efficiency of the color formation was very low, and the absorbance did not exhibit a linear behavior. Conversely, at higher concentrations, such as 0.24 mM - 0.60 mM octylamine, a significant improvement in linearity was observed with a linear fit (R^2 = 0.97). However, it should be noted that the curve did not intersect the origin. A non-linearity in absorbance at lower concentrations of amino acid standards with ninhydrin reagent and increased sensitivity at higher concentrations have been previously documented in the literature [90]. Even though the obtained linear curve did not pass through the origin, it was utilized as a calibration curve for the quantitative analysis in this study.

Moreover, there are several potential sources of errors and uncertainties in the performance of the ninhydrin assay. Firstly, it should be noted that there were only two replicate measurements performed for each sample, due to the time constraints of this project. Additionally, the samples of particles that are measured are highly diluted, reaching as low as 0.14 mg/mL of silica coated IONPs. These dilutions are determined based on prior dry weight concentrations of three replicates. It is crucial to consider that errors in these measurements could potentially introduce further inaccuracies and the calculations of amine contents in Figure 4.19 are normalized by the masses of these diluted samples. The particles were initially stored in water and then transferred to a dispersion containing 50% ethanol and 50% MQ-water. During this transfer process, there is a potential for the loss of particles and/or residual water containing free amine groups to be transferred along with the particles. These losses or remnants could affect the accuracy of the amine content measurements. Moreover, subsequent to the ninhydrin reaction, the solution was centrifuged, and only the colored supernatant without particles was measured using UV-Vis spectroscopy. This approach may result in the presence of remaining nanoparticles in the supernatant, which could potentially enhance the signal obtained during measurement.

Considering the potential sources of errors related to the approximate calculations and performance, including the limited number of replicate measurements, it is important to be aware of the un-

certainty associated with this study and the unexpectedly high quantities of surface amine groups observed. Therefore, it is recommended that future research focuses on further investigating the ninhydrin assay and potentially comparing it with other methods, such as conductometric titration, to validate and enhance the accuracy of the findings.

4.4 Magnetic Separability of Amine-Functionalized Silica Coated Iron Oxide Nanoparticles

To separate the silica-coated IONPs during the cleaning stages of the silanization procedure, centrifugation was employed, as described in Section 3.3. This method was chosen because it was observed that the particles did not separate effectively using a magnet, especially during the initial cleaning steps, leading to potential particle losses. However, magnetic separation is preferred as it enables the exclusion of non-magnetic particles and verifies the magnetic separability of the particles, which is crucial for the desired applications. Consequently, magnetic separation experiments were conducted to demonstrate the magnetic separability of the silica coated IONPs after cleaning and to investigate any potential correlation between solution pH, stability, and magnetic behavior.

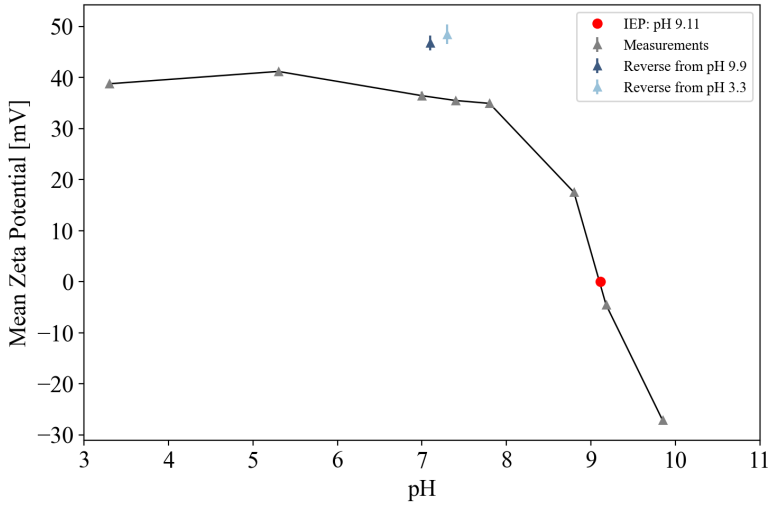

Figure 4.20: Mean zeta potential as a function of pH for experiment S100-25%-TD.

Magnetic separation experiments were conducted specifically for experiment S100-25%-TD. Initially, the zeta potential was measured while varying the pH of the sample, to determine the isoelectric point and stability of the sample. The sample was diluted with MQ-water and separated into two glass vials, both starting at pH 7. In one vial, the pH was raised by adding drops of diluted sodium hydroxide (NaOH) solution, while in the other vial, the pH was lowered by adding diluted hydrochloric acid (HCl). The zeta potential was then measured at different pH levels for

both vials, and Figure 4.20 shows the plotted curve between the measurements. In addition to the measurements taken at different pH levels, reverse measurements were performed at the pH endpoints and the isoelectric point (IEP) was determined to be at pH 9.11 from the plotted curve.

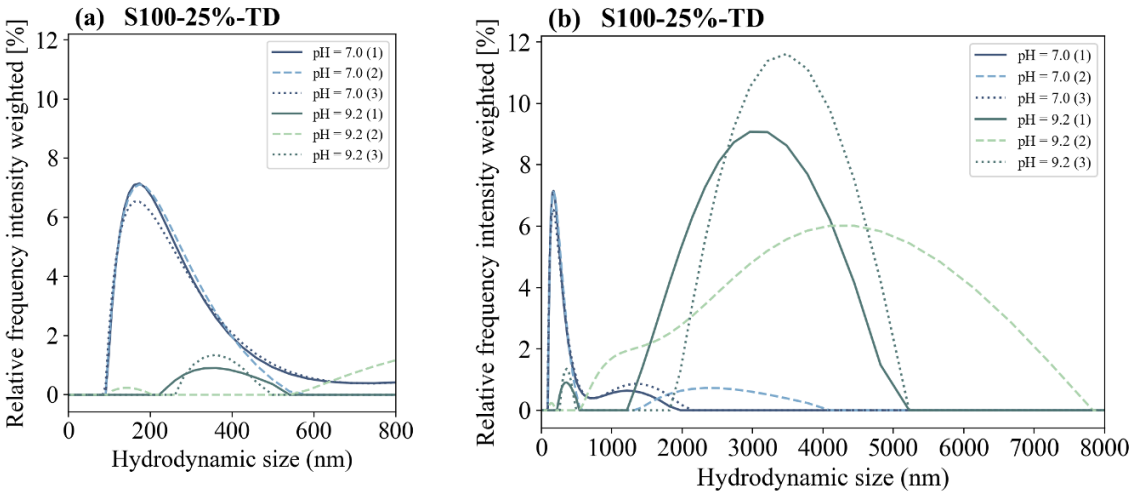

Figure 4.21: Measurements of hydrodynamic diameters for experiment S100-25%-TD at pH 7.0 and 9.2, with (a) and (b) illustrating the exact same measurements with different x-axis scales.

Furthermore, hydrodynamic size measurements were performed for all the different pH levels. Figure 4.21 demonstrates the hydrodynamic sizes based on three subsequent measurements at pH 7.0 and pH 9.2, with (a) and (b) illustrating the exact same measurements with different x-axis scales. At pH 7.0, where the zeta potential was measured to be +36.4 mV, the hydrodynamic size measurements show a prominent peak at around 200 nm. On the other hand, at a solution pH 9.2, the zeta potential was measured to be -4.5 mV, which is close to the isoelectric point, and significantly larger hydrodynamic sizes of about 3000 nm - 4000 nm were observed. This is most likely caused by particle aggregation due to a lack of electrostatic stabilization. Throughout the study, it was observed larger hydrodynamic sizes (>2000 nm) for pH levels close to the isoelectric point, whereas the mean hydrodynamic sizes were around 200 nm -350 nm for pH levels ranging from 7.8 to 3.3, as well as for pH 9.9 and the reverse pH measurements.

In parallel with the preformed zeta potential and hydrodynamic size measurements, an analysis of the magnetic separability of sample S100-25%-TD was conducted. Some undiluted sample was provided in two separate glass vials. In one vial, drops of diluted NaOH were added to elevate the pH, while in the other vial, drops of diluted HCl were added to decrease the pH. The sample was placed next to a magnet at various pH levels, and the time taken for complete separation of the sample was recorded. Figure 4.22 illustrates the magnetic separation process at pH 9.1, showing the separation progress at three different time intervals: (a) 30 seconds, (b) 40 seconds, and (c) 50 seconds. It was observed that the sample was separated within 40-50 seconds.

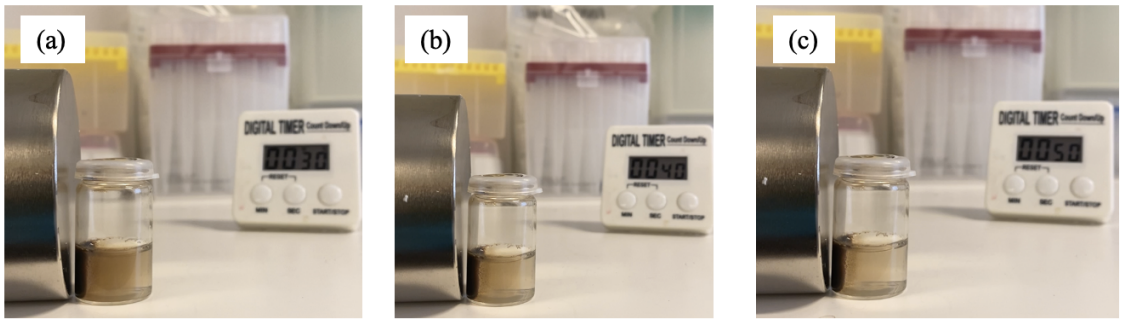

Figure 4.22: Magnetic separation for sample S100-25%-TD at pH 9.2, showing the separation progress as different time points: (a) 30 seconds, (b) 40 seconds and (c) 50 seconds.

Table 4.3: An overview of the magnetic separation times obtained at different pH levels and salt concentrations.

Solvent/Comment	Added	pH	Separation Time
Water	NaOH	10.0	3 - 3.5 mins
Water	NaOH	9.2	40 - 50 sec
Water	NaOH	8.4	2 - 3 mins
Water	-	7.1	2.5 - 3 mins
Water	HCl	6.5	3 - 4 mins
Water	HCl	5.5	3.5 - 4.5 mins
Water	HCl	4.1	3.5 - 4.5 mins
Water	HCl	3.0	4 - 5 mins
Water/Reverse from pH 10.0	HCl	7.1	1 - 2 mins
Water/Reverse from pH 3.0	NaOH	7.7	1 - 1.5 mins
0.1 M NaCl	-	7.4	1.5 - 2 mins
1.0 M NaCl	-	7.7	1 - 1.5 mins

Table 4.3 provides an overview of the separation times obtained at different pH values, with the initial pH at 7.1. The table includes separation times for the reverse pH measurements from the endpoints and back to the starting pH. Additionally, two measurements were conducted in which the silica coated IONPs were dispersed in solutions of 0.1 M and 1.0 M sodium chloride (NaCl). From Table 4.3, the magnetic separations are observed to be rapid when the pH is close to the isoelectric point, while the times increase as the pH deviates from it. Furthermore, the presence of NaCl in the solution, which influences the ionic strength of the system, is observed to enhance the speed of the separation process.

Consequently, based on all the obtained results, it is seen a clear trend in how the magnetic separability of the particles is correlated to the pH and ionic strength of the solution, and their impact

on particle stability. Near the determined IEP, the particles most likely tend to aggregate, which seems to strengthen their magnetic separability. Conversely, at pH values further away from the isoelectric point, the particles remain more stable in the solution, resulting in slower separability. Similarly, the presence of salt increases the ionic strength, which reduces the electrostatic interactions between the charged surfaces, leading to the formation of aggregates that are more easily separated. These findings may also help explain the poor magnetic separability observed immediately after the reaction stop in the synthesis. For instance, in the case of sample S100-15%-TD, the pH was measured to be 11.2 at the reaction stop, and subsequently 9.8 after one cleaning cycle with centrifuging. Although the curve in Figure 4.20 only depicts pH values up to 9.9, it is suggested that the particles were highly stable within the pH range of 11.2-9.8, based on the shape of the curve. This could potentially account for the observed difficulties in magnetic separation during the cleaning stages of the silica coated IONPs.

Chapter 5

Final Remarks

5.1 Conclusion

In the presented work, amine-functionalized silica coated iron oxide nanoparticles (IONPs) were synthesized by a co-condensation process of tetraethyl ortosilicate (TEOS) and 3-aminopropyl triethoxysilane (APTES) in the presence of IONPs. By systematically examining various reaction parameters, including the weight proportion of APTES of the total mass of TEOS and APTES, the type of IONPs, and volume of solvent, valuable insights concerning the particle properties have been discovered.

The results demonstrated that the presence of APTES plays a crucial role in a successful silanization process. Coating the IONPs solely with APTES resulted in incomplete coating and the formation of IONPs aggregates. However, the combination of APTES and TEOS led to the formation of individual particles of a multiple IONPs core-silica shell structure. Furthermore, the concentration of APTES in the silanization reaction significantly influenced the morphology of the particles. Higher APTES concentrations (> 3.9 mM) generated three distinct morphologies: large silica coated IONPs, silica particles, and aggregates of IONPs with a thin silica layer. In contrast, APTES concentrations ranging from 0.4 mM to 2.4 mM resulted in the formation of individual silica coated IONPs with sizes ranging from approximately 60 nm to 100 nm. In addition, it was found some larger aggregates of IONPs with a thin silica shell for some reaction conditions. Moreover, the effects of the type of IONPs and the volume of solvent utilized were explored. The IONPs were synthesized from both thermal decomposition and co-precipitation methods, and had different surface properties of Tri(ethylene glycol) (TREG) molecules and citrate ions, respectively. Interestingly, our findings revealed that the type of IONPs and solvent volume generally had minor effects on the particle properties compared to the weight proportion of APTES of the total mass of TEOS and APTES.

The hydrodynamic and dry size measurements of the silica coated IONPs showed no significant variations as the reaction parameters were varied. The silica coated IONPs demonstrated superparamagnetic behavior of saturation magnetization values ranging from 11.0 emu/g to 15.5 emu/g. In addition, it was discovered that the magnetic separability of the particles is dependent on the solution pH and its effect on electrostatic stability, demonstrating rapid magnetic separation near the isoelectric point. Analyses of the zeta potentials revealed positive surface charges of particles dispersed in water, spanning from 22.6±0.3 to 40.6±0.3 mV, which indicated the presence of APTES. The developed ninhydrin assay confirmed the existence of primary amine groups on the surfaces of the amine-functionalized silica coated IONPs. However, it was discovered unexpectedly high amine group contents up to 3322±74 μmol/g of free amine groups per mass of silica coated IONPs in comparison to existing literature. This raises concerns about the accuracy and reliability of the ninhydrin assay employed in this study, and further investigations are necessary.

In conclusion, the results of this study highlight the importance of the combination of APTES and TEOS in achieving a suitable coating and revealed the influence of the concentration of APTES on particle morphology. The findings provide valuable insights for controlling particle properties and created a framework for the production of potential amine-functionalized silica coated IONPs for applications in various fields.

5.2 Future Work

Based on the preliminary experiments, it was selected to use a variation of solvent volumes of 20 mL, 50 mL, and 100 mL, rather than larger volumes such as 150 mL. However, the characterizations of these experiments were limited and did not provide strong findings on which to base the decision on. Therefore, is recommended to conduct additional research on larger solvent volumes in the future to determine if there are any potential influences on the particle morphology.

Furthermore, is crucial to address the uncertainties associated with the ninhydrin assay by conducting further investigations and characterizations. For instance, the assay could be validated by using silica standards containing known quantities of amine groups. Additionally, the results obtained from the assay should be compared with other characterization methods that detect surface available groups such as conductometric titration.

Lastly, to ensure the statistical relevance and reproducibility of the obtained results, it is recommended to repeat the experiments and perform additional measurements. This will help verify the reliability of the findings and enhance the overall understanding of the effect of adjusting the reaction parameters.

Bibliography

[1] Z. Ali *et al.*, 'Fine-tuning of particle size and morphology of silica coated iron oxide nanoparticles,' *American Chemical Society*, vol. 62, no. 12, pp. 4831–4839, 2023.

[2] A. Ali *et al.*, 'Synthesis, characterization, applications, and challenges of iron oxide nanoparticles,' *Nanotechnology, Science and Applications*, vol. 9, pp. 49–67, 2016.

[3] A. M. Malekzadeh *et al.*, 'Design and construction of multifunctional hyperbranched polymers coated magnetite nanoparticles for both targeting magnetic resonance imaging and cancer therapy,' *Journal of Colloid and Interface Science*, vol. 490, pp. 64–73, 2017.

[4] Z.-Q. Zhang *et al.*, 'Thermosensitive/superparamagnetic iron oxide nanoparticle-loaded nanocapsule hydrogels for multiple cancer hyperthermia,' *Biomaterials*, vol. 106, pp. 13–23, 2016.

[5] C. Saikia *et al.*, 'Effect of crosslinker on drug delivery properties of curcumin loaded starch coated iron oxide nanoparticles,' *International Journal of Biological Macromolecules*, vol. 93, pp. 1121–1132, 2016.

[6] L. S. Arias *et al.*, 'Iron oxide nanoparticles for biomedical applications: A perspective on synthesis, drugs, antimicrobial activity, and toxicity,' *Antibiotics*, vol. 7, no. 2, 2018.

[7] C. Chircov *et al.*, 'Magnetic particles for advanced molecular diagnosis,' *Materials*, vol. 12, no. 2158, 2019.

[8] N. U. of Science and Technology. 'Ntnu covid-19 test.' (2020), [Online]. Available: `https://www.ntnu.edu/ntnu-covid-19-test` (visited on 21/04/2023).

[9] R. Abu-Huwaij *et al.*, 'Perceptive review on properties of iron oxide nanoparticles and their antimicrobial and anticancer activity,' *Systematic Reviews in Pharmacy*, vol. 11, no. 8, pp. 418–431, 2020.

[10] A. Raghunath *et al.*, 'Metal oxide nanoparticles as antimicrobial agents: A promise for the future,' *International Journal of Antimicrobial Agents*, vol. 49, no. 2, 2017.

[11] V. Fokina *et al.*, 'Size control of iron oxide nanoparticles synthesized by thermal decomposition methods,' *The Journal of Physical Chemistry*, vol. 126, no. 50, pp. 21 356–21 367, 2022.

[12] W. Wu *et al.*, 'Magnetic iron oxide nanoparticles: Synthesis and surface functionalization strategies,' *Nanoscale Research Letters*, vol. 3, no. 397, 2008.

[13] E. D. E. R. Hyde *et al.*, 'Colloidal silica particle synthesis and future industrial manufacturing pathways: A review,' *The American Chemical Society*, vol. 55, pp. 8891–8913, 2016.

[14] H. Li *et al.*, 'Functionalized silica nanoparticles: Classification, synthetic approaches and recent advances in adsorption applications,' *The Royal Society of Chemistry*, vol. 13, pp. 15 998–16 016, 2021.

[15] M. de Almeida *et al.*, 'Preparation and size-modulation of silica-coated maghemite nanoparticles,' *Journal of Alloys and Compounds*, vol. 500, no. 2, pp. 149–152, 2010.

[16] J. Mullin, *Crystallization*, 4. Butterworth-Heinemann, 2001, pp. 137–154.

[17] S. Bandyopadhyay, *Fabrication and Applications of Nanomaterials*. McGraw-Hill Education, 2019.

[18] A. B. Kristiansen *et al.*, 'Investigation of magnetite particle characteristics in relation to crystallization pathways,' *Powder Technology*, vol. 415, 2023.

[19] J.-P. Andreassen *et al.*, *New Perspectives on Mineral Nucleation and Growth*. Springer, 2017, ch. Classical and Nonclassical Theories of Crystal Growth, pp. 137–154.

[20] T. Panagiotou and R. J. Fisher, 'Enhanced transport capabilities via nanotechnologies: Impacting bioefficacy, controlled release strategies, and novel chaperones,' *Journal of Drug Delivery*, 2011.

[21] V. K. LaMer and R. H. Dinegar, 'Theory, production and mechanism of formation of monodispersed hydrosols,' *Journal of the American Chemical Society*, vol. 72, no. 11, pp. 4847–4854, 1950.

[22] N. T. K. Thanh *et al.*, 'Mechanisms of nucleation and growth of nanoparticles in solution,' *Chemical Reviews*, vol. 114, pp. 7610–7630, 2014.

[23] Y. Zhao, 'Quantum dots and doped nanocrystals: Synthesis, optical properties, and bioapplications,' 2013.

[24] J. Polte, 'Fundamental growth principles of colloidal metal nanoparticles - a new perspective,' *Royal Society of Chemistry*, vol. 17, pp. 6809–6830, 2015.

[25] S.-J. Park *et al.*, *Interface Science and Technology*. Academic Press, 2011, pp. 1–57.

[26] *Zeta potential*, `https://wiki.anton-paar.com/en/zeta-potential/`, Accessed: 2023-06-12.

[27] J. Jiang *et al.*, 'Characterization of size, surface charge, and agglomeration state of nanoparticle dispersions for toxicological studies,' *Journal of Nanoparticle Research*, vol. 11, pp. 77–89, 2009.

[28] M. R. Shah *et al.*, *Lipid-Based Nanocarriers for Drug Delivery and Diagnosis*. Elsevier Science, 2017, pp. 139–172.

[29] E. A. Campos *et al.*, 'Synthesis, characterization and applications of iron oxide nanoparticles - a short review,' *Journal of Aerospace Technology and Management*, vol. 7, no. 3, pp. 267–276, 2015.

[30] A. S. Teja *et al.*, 'Synthesis, properties, and applications of magnetic iron oxide nanoparticles,' *Progress in Crystal Growth and Characterization of Materials*, vol. 55, pp. 22–45, 2009.

[31] D. Levy *et al.*, 'Structure of magnetite (fe3o4) above the curie temperature: A cation ordering study,' *Physics and Chemistry of Minerals*, vol. 39, pp. 169–176, 2012.

[32] Q. Li *et al.*, 'Correlation between particle size/domain structure and magnetic properties of highly crystalline fe3o4 nanoparticles,' *Scientific Reports*, vol. 7, no. 9894, 2017.

[33] S. Zhang *et al.*, 'Superparamagnetic fe3o4 nanoparticles as catalysts for the catalytic oxidation of phenolic and aniline compounds),' *Journal of Hazardous Materials*, vol. 167, pp. 560–566, 2009.

[34] X. Ma *et al.*, 'Magnetite nanocrystals as anode electrode materials for rechargeable li-ion batteries,' *Journal of Nanoscience and Nanotechnology*, vol. 15, no. 9, pp. 7191–7194, 2015.

[35] M. G. El-Desouky *et al.*, 'Synthesis and characterization of porous magnetite nanosphere iron oxide as a novel adsorbent of anionic dyes removal from aqueous solution,' *Biointerface Research in Applied Chemistry*, vol. 11, no. 5, pp. 13 377–13 401, 2021.

[36] A.-G. Niculescu *et al.*, 'Magnetite nanoparticles: Synthesis methods – a comparative review,' *Methods*, vol. 199, pp. 16–27, 2022.

[37] M. O. Besenhard *et al.*, 'Continuous production of iron oxide nanoparticles via fast and economical high temperature synthesis,' *Reaction Chemistry and Engineering*, vol. 5, pp. 1474–1483, 2020.

[38] A. Sharma *et al.*, 'Magnetic nanoparticles to unique dna tracers: Effect of functionalization on physico-chemical properties,' *Scientific Reports*, vol. 16, no. 24, 2021.

[39] A. Lassenberger *et al.*, 'Monodisperse iron oxide nanoparticles by thermal decomposition: Elucidating particle formation by second-resolved in situ small-angle x-ray scattering,' *Chemistry of materials*, vol. 29, no. 10, pp. 4511–4522, 2017.

[40] D. Maity *et al.*, 'Studies of magnetite nanoparticles synthesized by thermal decomposition of iron (iii) acetylacetonate in tri(ethylene glycol),' *Chemistry of materials*, vol. 321, no. 19, pp. 3093–3098, 2009.

[41] S. I. C. J. Palma *et al.*, 'Effects of phase transfer ligands on monodisperse iron oxide magnetic nanoparticles,' *Journal of Colloid and Interface Science*, vol. 437, pp. 147–155, 2015.

[42] J. Wan *et al.*, 'Monodisperse water-soluble magnetite nanoparticles prepared by polyol process for high-performance magnetic resonance imaging,' *Chemical Communications*, no. 47, pp. 5004–5006, 2007.

[43] S. Laurent *et al.*, 'Magnetic iron oxide nanoparticles: Synthesis, stabilization, vectorization, physicochemical characterizations, and biological applications,' *Chemical Reviews*, vol. 110, no. 4, 2010.

[44] P. J. Vikesland *et al.*, 'Aggregation and sedimentation of magnetite nanoparticle clusters,' *The Royal Society of Chemistry*, vol. 3, pp. 567–577, 2016.

[45] S. P. Schwaminger *et al.*, 'Oxidation of magnetite nanoparticles: Impact on surface and crystal properties,' *The Royal Society of Chemistry*, vol. 19, no. 1, pp. 246–255, 2017.

[46] N. Zhu *et al.*, 'Surface modification of magnetic iron oxide nanoparticles,' *Nanomaterials*, vol. 8, no. 10, 2018.

[47] Z. Shaterabadi *et al.*, 'High impact of in situ dextran coating on biocompatibility, stability and magnetic properties of iron oxide nanoparticles,' *Materials Science and Engineering*, vol. 75, pp. 947–956, 2017.

[48] P. Shete *et al.*, 'Magnetic chitosan nanocomposite for hyperthermia therapy application: Preparation, characterization and in vitro experiments,' *Applied Surface Science*, vol. 288, pp. 149–157, 2014.

[49] M. Anbarasu *et al.*, 'Synthesis and characterization of polyethylene glycol (peg) coated fe3o4 nanoparticles by chemical co-precipitation method for biomedical applications,' *Spectrochimica Acta Part A: Molecular and Biomolecular Spectroscopy*, vol. 135, pp. 536–539, 2015.

[50] Y. Jin *et al.*, 'Efficient bacterial capture with amino acid modified magnetic nanoparticles,' *Water Research*, vol. 50, pp. 124–134, 2014.

[51] J.-F. Lin *et al.*, 'Linear birefringence and dichroism in citric acid coated fe3o4 magnetic nanoparticles,' *Journal of Magnetism and Magnetic Materials*, vol. 372, pp. 147–158, 2014.

[52] V. Sreeja *et al.*, 'Water-dispersible ascorbic-acid-coated magnetite nanoparticles for contrast enhancement in mri,' *Applied Nanoscience*, vol. 5, pp. 435–441, 2014.

[53] R. G. Digigow *et al.*, 'Preparation and characterization of functional silica hybrid magnetic nanoparticles,' *Journal of Magnetism and Magnetic Materials*, vol. 362, pp. 72–79, 2014.

[54] J. Liu *et al.*, 'One-pot synthesis of mesoporous interconnected carbon-encapsulated fe3o4 nanospheres as superior anodes for li-ion batteries,' *The Royal Society of Chemistry*, vol. 2, pp. 2262–2265, 2012.

[55] C. Li *et al.*, 'Gold-coated fe3o4 nanoroses with five unique functions for cancer cell targeting, imaging and therapys,' *Advanced Functional Materials*, vol. 24, no. 12, pp. 1772–1780, 2014.

[56] G. Gao *et al.*, 'Superparamagnetic fe3o4-ag hybrid nanocrystals as a potential contrast agent for ct imaging,' *CrystEngComm,*, vol. 14, no. 22, pp. 7556–7559, 2012.

[57] J. Saffari *et al.*, 'Sonochemical synthesis of fe3o4/zno magnetic nanocomposites and their application in photo-catalytic degradation of various organic dyes,' *CrystEngComm*, vol. 26, pp. 9591–9599, 2015.

[58] M. Abbas *et al.*, 'Highly stable- silica encapsulating magnetite nanoparticles (fe3o4/sio2) synthesized using single surfactantless- polyol process,' *Ceramics International*, vol. 40, no. 1, pp. 1379–1385, 2014.

[59] *Crystalline silica: The science*, `https://safesilica.eu/crystalline-silica-the-science/`, Accessed: 2023-02-28.

[60] A. A. Nayl *et al.*, 'Recent progress in the applications of silica-based nanoparticles,' *the Royal Society of Chemistry*, vol. 12, pp. 13 706–13 726, 2022.

[61] Stöber *et al.*, 'Controlled growth of monodisperse silica spheres in the micron size range,' *Journal of Colloid and Interface Science*, vol. 26, pp. 62–69, 1968.

[62] Y. Han *et al.*, 'Unraveling the growth mechanism of silica particles in the stöber method: In situ seeded growth model,' *American Chemical Society*, vol. 33, pp. 5879–5890, 2017.

[63] P. P. Ghimire *et al.*, 'Renaissance of stöber method for synthesis of colloidal particles: New developments and opportunities,' *Journal of Colloid and Interface Science*, vol. 584, pp. 838–865, 2021.

[64] A. H. Bari *et al.*, 'Understanding the role of solvent properties on reaction kinetics for synthesis of silica nanoparticles,' *Chemical Engineering Journal*, vol. 398, 2020.

[65] G. Bogush *et al.*, 'Studies of the kinetics of the precipitation of uniform silica particles through the hydrolysis and condensation of silicon alkoxides,' *American Chemical Society*, vol. 142, no. 1, pp. 1–18, 1991.

[66] H. Giesche, 'Synthesis of monodispersed silica powders i. particle properties and reaction kinetics,' *Journal of the European Ceramic Society*, vol. 14, no. 3, pp. 189–204, 1994.

[67] E. Mine *et al.*, 'Direct coating of gold nanoparticles with silica by a seeded polymerization technique,' *Journal of Colloid and Interface Science*, vol. 264, no. 2, pp. 385–390, 2003.

[68] F. Boccafoschi *et al.*, *Functionalised Cardiovascular Stents*. Woodhead Publishing, 2018, pp. 305–318.

[69] F. Ahangaran *et al.*, 'Recent advances in chemical surface modification of metal oxide nanoparticles with silane coupling agents: A review,' *Advances in Colloid and Interface Science*, vol. 286, 2020.

[70] Y. Zhang *et al.*, 'Effects of vinyl functionalized silica particles on thermal and mechanical properties of liquid silicone rubber nanocomposites,' *Polymers*, vol. 15, no. 5, 2023.

[71] K. Möller *et al.*, 'Colloidal suspensions of mercapto-functionalized nanosized mesoporous silica,' *Journal of Materials Chemistry*, vol. 17, pp. 624–631, 2007.

[72] M. Oszust *et al.*, 'Adsorption of l-histidine onto functionalized mesoporous sba-15organosilicas,' *Adsorption Science and Technology*, vol. 33, no. 6-8, 2015.

[73] D. Zhu *et al.*, *Handbook of Waterborne Coatings*. Elsevier, 2020, pp. 1–27.

[74] M. Barczak, 'Functionalization of mesoporous silica surface with carboxylic groups by meldrum's acid and its application for sorption of proteins,' *Journal of Porous Materials*, vol. 26, pp. 291–300, 2019.

[75] H. Li *et al.*, 'Functionalized silica nanoparticles: Classification, synthetic approaches and recent advances in adsorption applications,' *Nanoscale*, vol. 13, no. 38, pp. 15 998–16 016, 2021.

[76] M. Sypabekova *et al.*, 'Review: 3-aminopropyltriethoxysilane (aptes) deposition methods on oxide surfaces in solution and vapor phases for biosensing applications,' *Biosensors*, vol. 13, no. 36, 2023.

[77] Y. Sun *et al.*, 'Quantification of amine functional groups on silica nanoparticles: A multi-method approach,' *The Royal Society of Chemistry*, vol. 1, pp. 1598–1607, 2019.

[78] K. E. Sapsford *et al.*, 'Functionalizing nanoparticles with biological molecules: Developing chemistries that facilitate nanotechnology,' *Chemcial Reviews*, vol. 113, no. 3, 19042074, 2013.

[79] I. Rahman *et al.*, 'Synthesis of organo-functionalized nanosilica via a co-condensation modification using -aminopropyltriethoxysilane (aptes),' *Ceramics International*, vol. 35, no. 5, pp. 1883–1888, 2009.

[80] A. V. Blaaderen *et al.*, 'Synthesis and characterization of monodisperse colloidal organo-silica spheres,' *Journal of Colloid and Interface Science*, vol. 156, pp. 1–18, 1993.

[81] S. Chen *et al.*, 'Sol-gel synthesis and microstructure analysis of amino-modified hybrid silica nanoparticles from aminopropyltriethoxysilane and tetraethoxysilane,' *Journal of the American Ceramic Society*, vol. 92, no. 9, pp. 2074–2082, 2009.

[82] J.-F. Dechezelles *et al.*, 'Hybrid raspberry microgels with tunable thermoresponsive behavior,' *Soft Matter*, vol. 9, no. 10, pp. 2798–2802, 2013.

[83] S. Kralj *et al.*, 'Controlled surface functionalization of silica-coated magnetic nanoparticles with terminal amino and carboxyl groups,' *Journal of Nanoparticle Research*, vol. 13, pp. 2829–2841, 2011.

[84] F. Kunc *et al.*, 'Quantification and stability determination of surface amine groups on silica nanoparticles using solution nmr,' *Analytical Chemistry*, vol. 90, no. 22, pp. 13 322–13 330, 2018.

[85] E. Soto-Cantu *et al.*, 'Synthesis and rapid characterization of amine-functionalized silica,' *Langmuir*, vol. 28, no. 13, pp. 5562–5569, 2012.

[86] Y. Sun *et al.*, 'Quantification of amine functional groups on silica nanoparticles: A multimethod approach,' *Nanoscale Advances*, vol. 1, pp. 1598–1607, 2019.

[87] V. C. Karade *et al.*, 'Aptes monolayer coverage on self-assembled magnetic nanospheres for controlled release of anticancer drug nintedanib,' *Scientific Reports*, vol. 11, no. 5674, 2021.

[88] *Product info lumisizer*, `https://www.lum-gmbh.com/lumisizer_en.html`, Accessed: 2023-05-29.

[89] Z. Ali, 'Insights into growth mechanism, control of particle size and particle size distribution of silica coated iron oxide nanoparticles,' *Deparment of Chemical Engineering, Norwegian University of Science and Technology*, 2020.

[90] G. Haeger *et al.*, 'A convenient ninhydrin assay in 96-well format for amino acid-releasing enzymes using an air-stable reagent,' *Analytical Biochemistry*, vol. 654, 2022.

Appendix A

Silanization Reaction Conditions

A.0.1 Theoretical Mass of Obtained Silica

Theoretical mass of obtained silica, m_{Silica}, is calculated by Equation A.1 [53]:

$$m_{\text{Silica}} = \left(\frac{m_{\text{TEOS}}}{M_{\text{TEOS}}} + \frac{m_{\text{APTES}}}{M_{\text{APTES}}} \right) \cdot M_{\text{Silica}} \tag{A.1}$$

Where m_{TEOS} is the mass of TEOS, M_{TEOS} is the molar mass of TEOS, m_{APTES} is the mass of APTES, M_{APTES} is the molar mass of APTES and M_{Silica} is the molar mass of silica.

All the mass ratio of TEOS to APTES is determined such as the obtained theoretical mass of silica is 49 mg. For example, 140 μL TEOS and 46 μL APTES gives:

$$m_{\text{TEOS}} = 933 \text{ mg/mL} \cdot 140 \cdot 10^{-3} \text{ mL} = 131 \text{ mg}$$

$$m_{\text{APTES}} = 946 \text{ mg/mL} \cdot 46 \cdot 10^{-3} \text{ mL} = 43 \text{ mg}$$

where densities are found from their specific material description from Sigma-Aldrich.

$$m_{\text{Silica}} = \left(\frac{0.131 \text{ g TEOS}}{208.33 \text{ g/mol TEOS}} + \frac{0.043 \text{ g APTES}}{221.37 \text{ g/mol APTES}} \right) \cdot 60.08 \text{ g/mol Silica}$$

$$m_{\text{Silica}} = 49 \text{ mg}$$

Table A.1: An overview of quantities of chemicals used for each experiment.

Sample [-]	EtOH [mL]	Water [mL]	TEOS [uL]	APTES [uL]	Ammonia [uL]	IONPs [mg]	IONPs Type [-]	Flask [mL]
S20-5%-TD	16	4	175	9	200	10	TD	100
S20-15%-TD	16	4	158	28	200	10	TD	100
S20-25%-TD	16	4	140	46	200	10	TD	100
S50-5%-TD	40	10	175	9	500	10	TD	100
S50-15%-TD	40	10	158	28	500	10	TD	100
S50-25%-TD	40	10	140	46	500	10	TD	100
S60-15%-TD	48	12	158	28	600	10	TD	100
S100-5%-TD	80	20	175	9	1000	10	TD	250
S100-15%-TD	80	20	158	28	1000	10	TD	250
S100-25%-TD	80	20	140	46	1000	10	TD	250
S20-5%-CP	16	4	175	9	200	10	CP	100
S20-15%-CP	16	4	158	28	200	10	CP	100
S20-25%-CP	16	4	140	46	200	10	CP	100
S50-5%-CP	40	10	175	9	500	10	CP	100
S50-15%-CP	40	10	158	28	500	10	CP	100
S50-25%-CP	40	10	140	46	500	10	CP	100
S60-15%-CP	48	12	158	28	600	10	CP	100
S100-5%-CP	80	20	175	9	1000	10	CP	250
S100-15%-CP	80	20	158	28	1000	10	CP	250
S100-25%-CP	80	20	140	46	1000	10	CP	250
S100-100%-TD	80	20	0	193	1000	10	TD	250
S100-100%-CP	80	20	0	193	1000	10	CP	250
S100-0%-TD	80	20	184	0	1000	10	TD	250
S100-0%-CP	80	20	184	0	1000	10	CP	250

Appendix B

Scanning Transmission Electron Spectroscopy Images

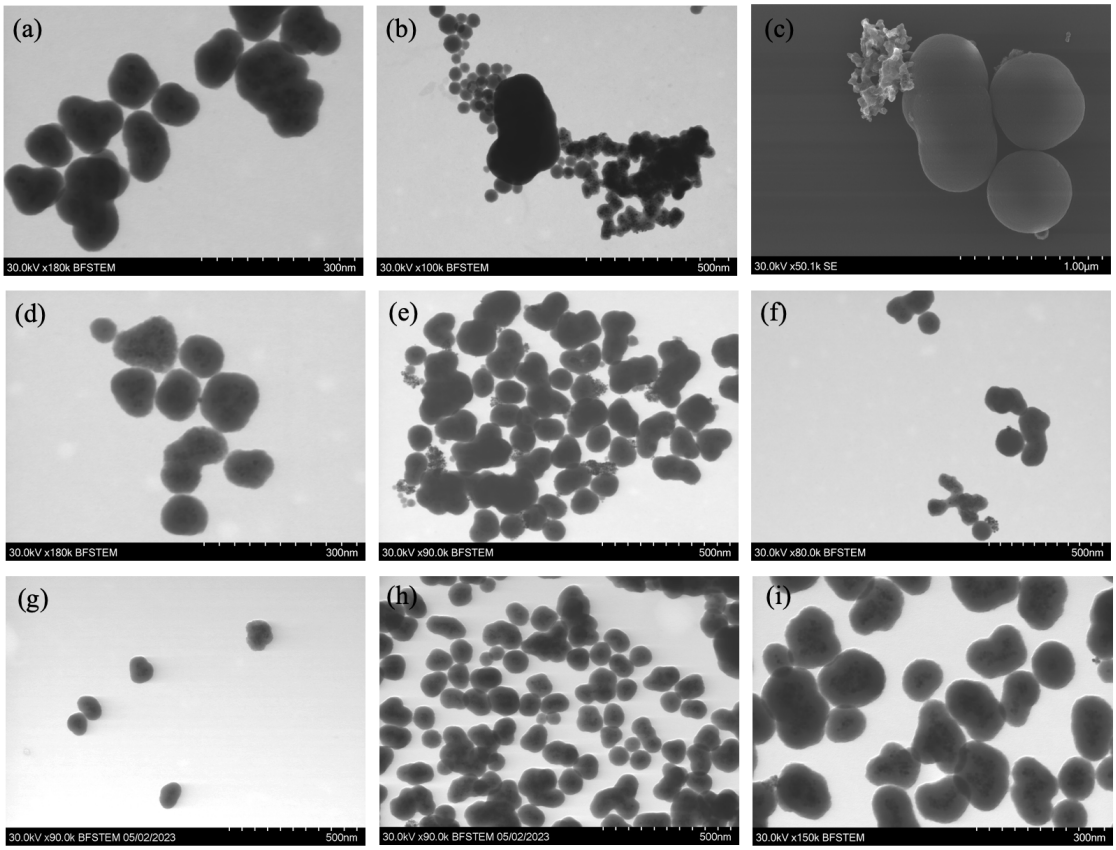

Figure B.1: TEM images of experiment (a) S20-5%-TD, (b) S20-15%-TD, (c) S20-25%-TD, (d) S50-5%-TD, (e) S50-15%-TD, (f) S50-25%-TD, (g) S100-5%-TD, (h) S100-15%-TD, (i) S100-25%-TD.

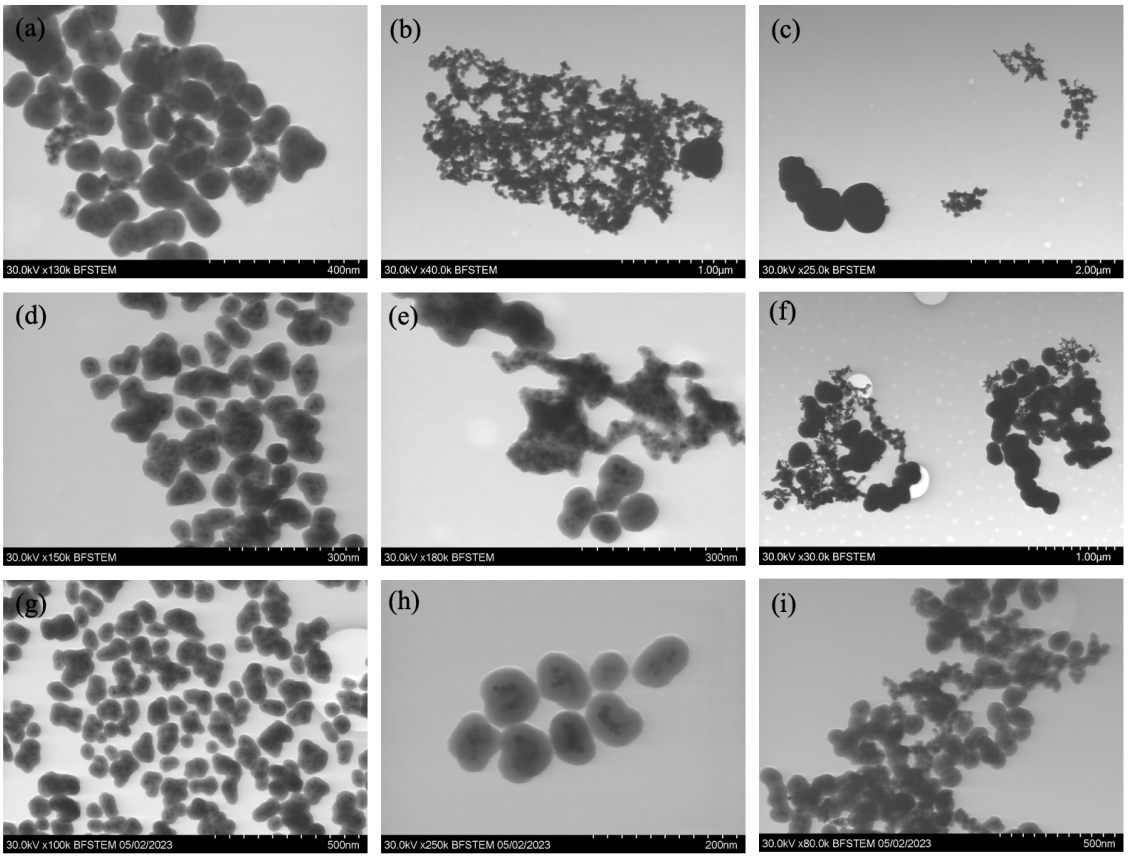

Figure B.2: TEM images of experiment (a) S20-5%-CP, (b) S20-15%-CP, (c) S20-25%-CP, (d) S50-5%-CP, (e) S50-15%-CP, (f) S50-25%-CP, (g) S100-5%-CP, (h) S100-15%-CP, (i) S100-25%-CP.

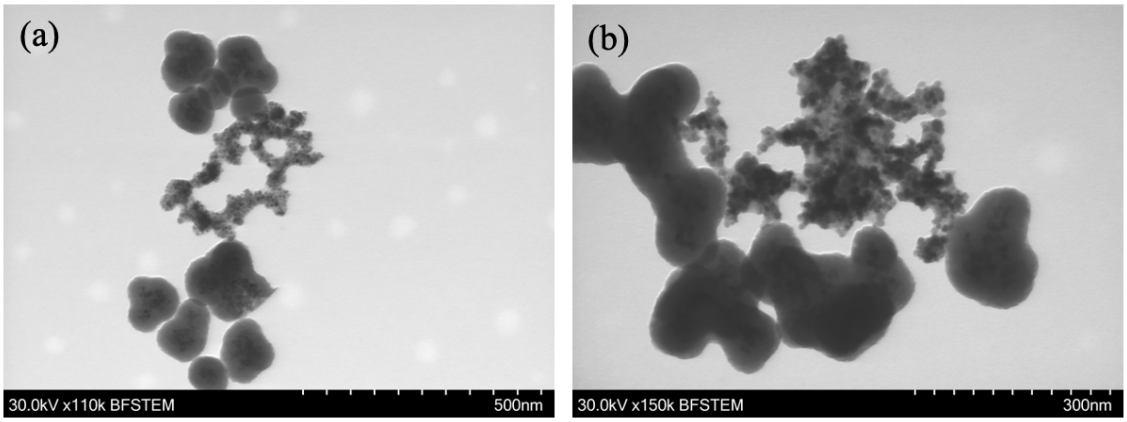

Figure B.3: TEM images of center points experiments (a) S60-15%-TD and (b) S60-15%-CP.

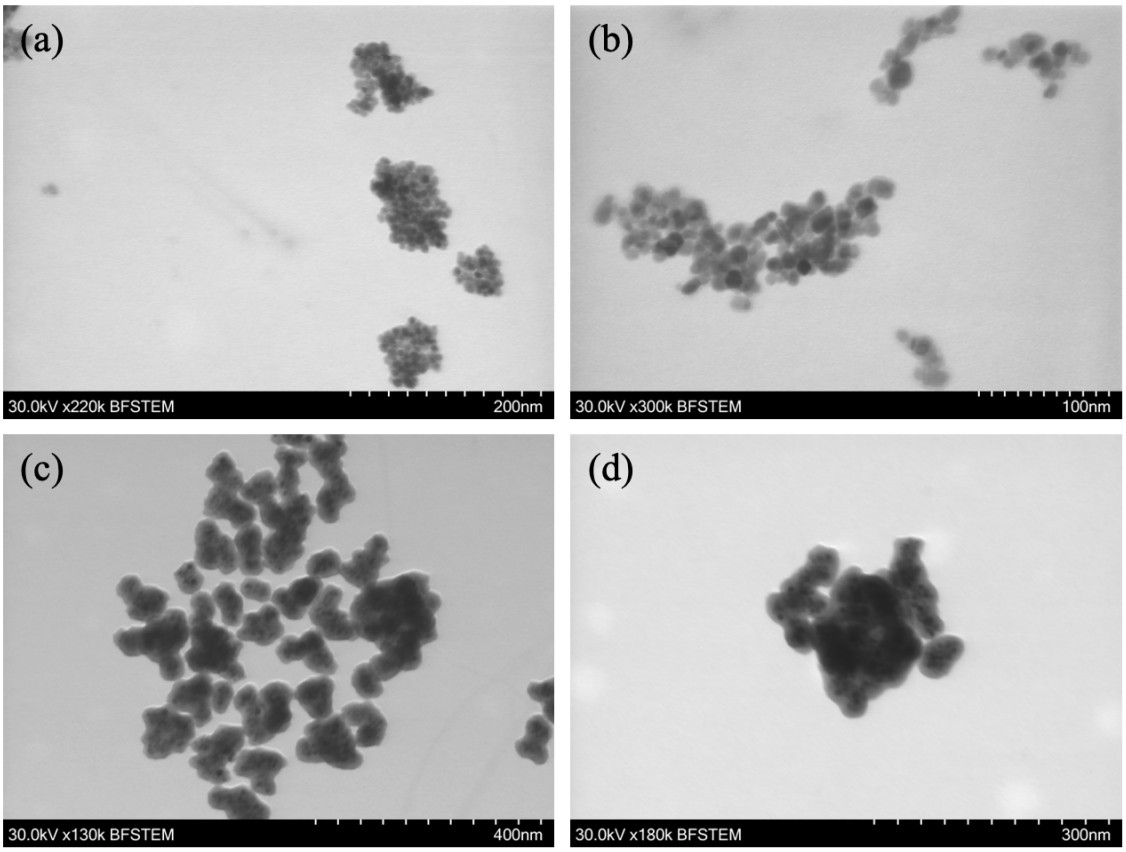

Figure B.4: TEM images of control experiments (a) S100-100%-TD, (b) S100-100%-CP, (c) S100-0%-TD and (d) S100-0%-CP.

Appendix C

Calculations of Quantity of Amine Groups

The specific surface area (SSA) for a spherical particle was calculated from Equation C.1 [87]:

$$SSA = \frac{3}{\rho \cdot \frac{d}{2}} \tag{C.1}$$

where d is the diameter and ρ is the density of the material. The average bright-field TEM diameter and the density of silica 2.65 g/cm^3 were utilized.

As reported by the study of Karade *et al.* [87], the calculation of fractional monolayer coverage of amine groups is given by Equation C.2:

$$\text{Fractional monolayer coverage} = \frac{\text{total amine from ninhydrin assay}}{\text{estimated amine for monolayer coverage}} \cdot 100\% \tag{C.2}$$

assuming four aminopropylsilanes per nm^2 for monolayer coverage of APTES.

For example, for experiment S100-5%-TD, where the mean TEM diameter was measured to be 85 nm, SSA is calculated to be:

$$SSA = \frac{3 \cdot 2}{2.65 \text{ g/cm}^3 \cdot 85 \text{ nm}} \cdot \frac{10^{21} \text{ nm}^3}{1 \text{ cm}^3} = 2.66 \cdot 10^{19} \text{ nm}^2/\text{g}$$

The mean amine content for experiment S100-5%-TD obtained from the ninhydrin assay was measured to be 232 μmol/g. Fractional monolayer coverage assuming four aminopropylsilanes per nm^2 are accordingly calculated to be:

$$\text{Fractional monolayer coverage} = \frac{232 \cdot 10^{-6}\ \text{mol/g} \cdot 6.022 \cdot 10^{23}\ \text{mol}^{-1}}{4\ \text{nm}^{-2} \cdot 2.66 \cdot 10^{19}\ \text{nm/g}} \cdot 100\% = 131\%$$

which corresponds to 1.31 times monolayer coverage. Considering that the particles also containes IONPs, which have a greater density than silica, the SSA would decrease and the calculations would yield an even higher coverage of amine groups.

Appendix D

Calibration curves of Octylamine

Figure D.1 shows absorbance measurement points of different octylamine concentrations. The measurement points of the same colors are obtained subsequently on the same day. Linear regression of points from 0.24 mM - 0.60 mM ocylamine was observed to give a linear curve.

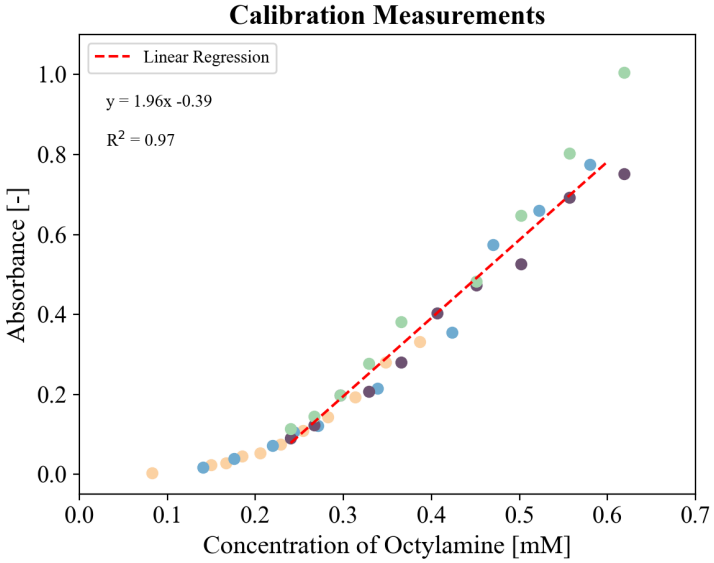

Figure D.1: Calibration measurements of octylamine.

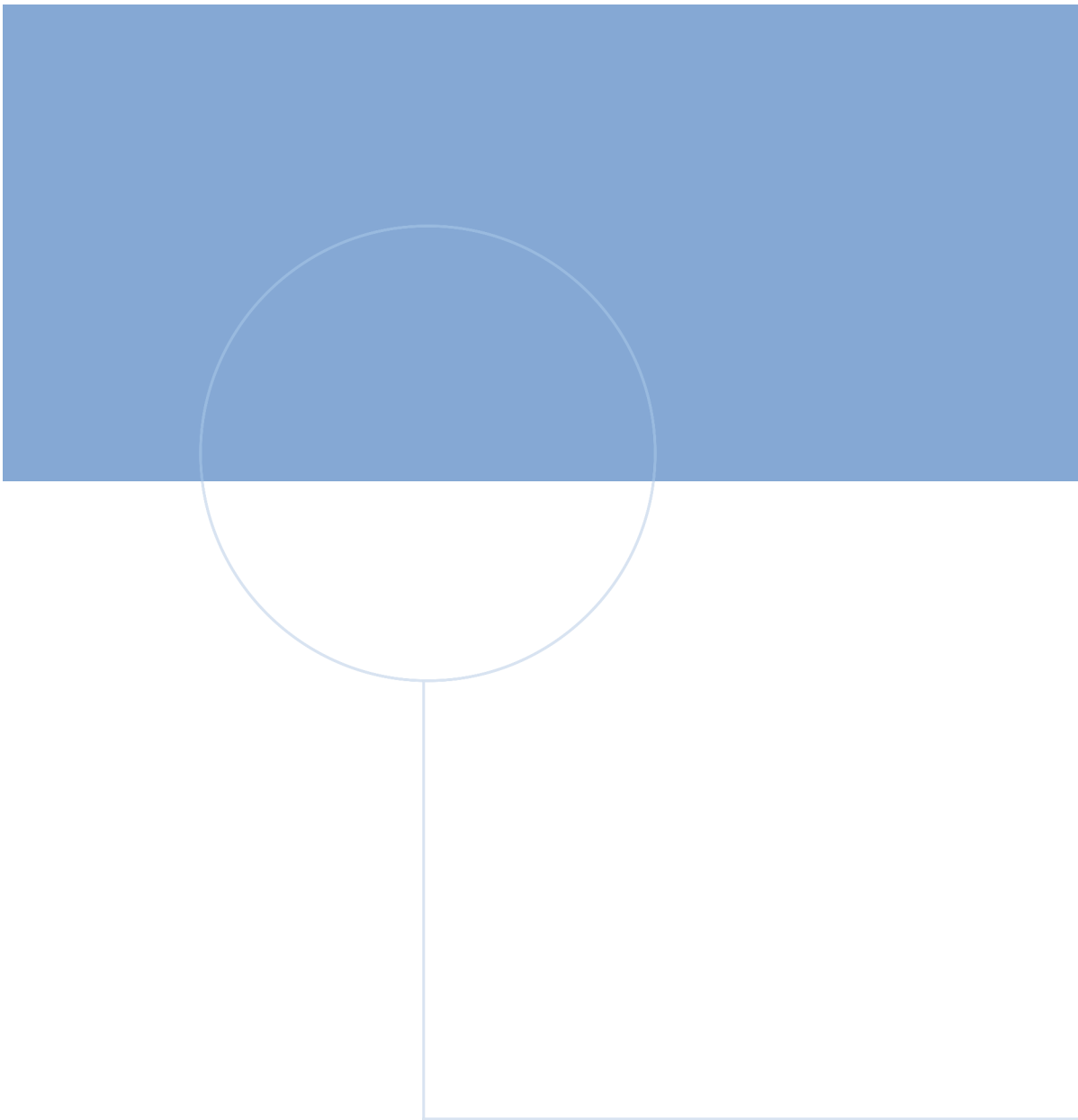

NTNU

Norwegian University of
Science and Technology